

## **Automated cell tracking identifies mechanically-oriented cell divisions during *Drosophila* axis elongation**

Michael F. Z. Wang<sup>1,2</sup>, Miranda Hunter<sup>2,3</sup>, Gang Wang<sup>1</sup>, Christopher McFaul<sup>1,2</sup>, Christopher M. Yip<sup>1</sup> and Rodrigo Fernandez-Gonzalez<sup>1,2,3,4,\*</sup>

<sup>1</sup> Institute of Biomaterials and Biomedical Engineering, University of Toronto, Toronto, ON, Canada M5S 3G9.

<sup>2</sup> Ted Rogers Centre for Heart Research, University of Toronto, Toronto, ON, Canada M5G 1M1.

<sup>3</sup> Department of Cell and Systems Biology, University of Toronto, Toronto, ON, Canada M5S 3G5.

<sup>4</sup> Developmental and Stem Cell Biology Program, The Hospital for Sick Children, Toronto, ON, Canada M5G 1X8.

**Keywords:** image analysis, machine learning, time-lapse microscopy, morphogenesis, oriented cell division, laser ablation

\* Corresponding author:

email: [rodrigo.fernandez.gonzalez@utoronto.ca](mailto:rodrigo.fernandez.gonzalez@utoronto.ca)

phone: 416-978-7368

fax: 416-978-4317

## Abstract

Embryos extend their anterior-posterior (AP) axis in the conserved process of axis elongation. *Drosophila* axis elongation occurs in an epithelial monolayer, the germband, and is driven by cell intercalation, cell shape changes, and oriented cell divisions at the posterior germband. Anterior germband cells also divide during axis elongation. We developed image analysis and pattern recognition methods to track dividing cells from confocal microscopy movies in a generally-applicable approach. Mesectoderm cells, forming the ventral midline, divided parallel to the AP axis, while lateral cells displayed a uniform distribution of division orientations. Mesectoderm cells did not intercalate and sustained increased AP strain before cell division. After division, mesectoderm cell density increased along the AP axis, thus relieving strain. We used laser ablation to isolate mesectoderm cells from other tissues. Uncoupling the mesectoderm from intercalating cells did not affect cell division orientation. Conversely, separating the mesectoderm from the anterior and posterior poles of the embryo resulted in uniformly-oriented divisions. Our data suggest that mesectoderm cells align their division angle to reduce strain caused by mechanical forces along the AP axis of the embryo.

## Introduction

Axis elongation is a conserved morphogenetic process in which embryos extend their anterior-posterior (AP) axis. In *Drosophila*, axis elongation occurs in the germband, an epithelial monolayer that gives rise to the epidermis and the central nervous system (Hartenstein and Campos-Ortega, 1985). During axis elongation, the germband extends by more than twofold (Fig. S1), in a process mainly driven by directional cell rearrangements (Irvine and Wieschaus, 1994; Bertet et al., 2004; Zallen and Wieschaus, 2004; Blankenship et al., 2006). Cells intercalate between their dorsal or ventral neighbours, thus promoting AP tissue elongation.

The directionality of cell intercalation during germband extension is controlled by AP patterning (Irvine and Wieschaus, 1994). AP patterning establishes tissue-level planar polarity of cytoskeletal and junctional proteins (Zallen and Wieschaus, 2004; Blankenship et al., 2006; Pare et al., 2014). Actin and myosin localize preferentially to cell-cell contacts perpendicular to the AP axis, generating contractile forces that promote systematic disassembly of cell interfaces (Bertet et al., 2004; Zallen and Wieschaus, 2004; Blankenship et al., 2006; Rauzi et al., 2008; Fernandez-Gonzalez et al., 2009). At the same time, anisotropic pulsatile behaviours of germband cells and endoderm internalization in the posterior pole of the embryo produce AP-oriented deformation (strain) that causes cell elongation (Butler et al., 2009; Fernandez-Gonzalez and Zallen, 2011; Sawyer et al., 2011) and facilitates polarized assembly of new cell-cell contacts parallel to the AP axis, thus driving tissue extension (Collinet et al., 2015; Lye et al., 2015; Yu and Fernandez-Gonzalez, 2016).

Oriented cell divisions contribute to germband extension (da Silva and Vincent, 2007). Cell divisions are predominantly parallel to the AP axis at the posterior tip of the extending germband, and inhibiting cell division slows down germband elongation. More anteriorly, lateral germband cells and mesectoderm cells also divide, forming distinct mitotic domains (Foe, 1989). Mesectoderm cells form the ventral midline, separate the ectoderm from the internalized mesoderm, and eventually form a discrete set of glia and neurons (Jacobs and Goodman, 1989; Klambt et al., 1991). It is currently unknown if the divisions in the anterior germband are oriented during *Drosophila* axis elongation.

Mechanical forces can orient cell division in developing animals (Le Goff and Lecuit, 2011; Mao et al., 2011; Campinho et al., 2013; Mao et al., 2013; Bosveld et al., 2016). In the *Drosophila* embryo, defects in AP patterning disrupt cell division orientation on the posterior germband (da Silva and Vincent, 2007). Notably, defective AP patterning disrupts both AP and DV oriented forces and cell intercalation (Irvine and Wieschaus, 1994; Zallen and Wieschaus, 2004; Blankenship et al., 2006; Fernandez-Gonzalez et al., 2009; Fernandez-Gonzalez and Zallen, 2011; Collinet et al., 2015). Thus, it is not clear if oriented cell divisions during germband extension are cell-autonomously regulated by AP patterning, or if the orientation of cell division is non-autonomously determined by the effect of AP patterning on the distribution of mechanical forces.

Investigation of cellular dynamics from microscopy images requires cell delineation and tracking. The watershed algorithm (Beucher, 1992), a region growing method, is often used as the basis for cell segmentation from fluorescence microscopy images (Aigouy et al., 2010; Fernandez-Gonzalez and Zallen, 2011; Mashburn et al., 2012; Mosaliganti et al., 2012; Leung and Fernandez-Gonzalez, 2015). However, the success of watershed-based approaches critically depends on the identification of a single seed point within each cell to be segmented. Otherwise, segmentation errors occur and the resulting polygons need to be manually corrected in a process that is time-consuming and error-prone. Tracking is often accomplished by linking cells frame-to-frame based on cell overlap (Aigouy et al., 2010; Mashburn et al., 2012; Guirao et al., 2015). To further refine tracking and compensate for data with low temporal resolution, morphological features -such as cell size or shape-, and topographical information, including the identity of cell neighbours, can be used (Etournay et al., 2016). However, these tracking methods depend heavily on the accuracy of the segmentation. Alternatively, cell tracking can be made segmentation-independent by matching image sub-regions instead of individual cells. Optic flow uses the cross-correlation of two images to calculate local similarities (Raffel et al., 1998), and can be used to track cells based on matching fluorescence patterns (Mosaliganti et al., 2012; Yu and Fernandez-Gonzalez, 2016). Segmentation-independent methods can be computationally expensive when fine spatial or temporal sampling are necessary, for instance in the case of rapidly moving cells. Thus, integrating segmentation and tracking can be beneficial for the effectiveness of both approaches (Wahlby et al., 2004; Schiegg et al., 2015).

Here, we use *in vivo* confocal microscopy to investigate cell division dynamics in the anterior germband during *Drosophila* axis elongation. We develop a novel image analysis method for cell delineation and tracking, and we use machine learning to automatically identify dividing cells. We find that, in contrast to lateral germband cells, mesectoderm (ventral) cells divide parallel to the AP axis of the embryo. Oriented cell divisions increase cell density along the AP axis on the ventral midline of the embryo, where cells do not intercalate. We use laser ablation to mechanically isolate ventral cells from intercalating cells or from the anterior-posterior poles of the embryo, and we find that AP-oriented forces from the embryonic poles determine the direction of cell division. We propose that tension parallel to the AP axis orients cell division in the ventral germband, thus increasing AP cell density, reducing cell strain and facilitating axis elongation.

## Results

### Seed-editing improves watershed-based cell delineation

To quantify cellular dynamics from confocal microscopy images of embryos expressing a fluorescently-tagged cell outline marker, we developed an algorithm integrating cell delineation (segmentation) and tracking. To automatically identify one seed per cell, we used adaptive thresholding to separate membrane and cytoplasmic pixels, followed by a distance transform (Fernandez-Gonzalez and Zallen, 2011; Leung and Fernandez-Gonzalez, 2015). The local maxima of the distance transform represented the cytoplasmic pixels furthest away from the cell membrane and were used as seeds. In images of *Drosophila* embryos expressing Gap43:mCherry (Martin et al., 2010) and undergoing axis elongation,  $95.7 \pm 1.2\%$  of the seeds generated by our approach inside the embryo were correctly placed as the only seed within one cell (Fig. 1A). Errors in seed detection resulted in over- or undersegmentation of one or more cells (Fig. 1A'). Furthermore, our method also placed seeds in the background or within cells that were not completely included in the field of view. As a consequence, only  $74.0 \pm 5.3\%$  of the polygons resulting from watershed-based seed expansion represented properly segmented cells (Fig. 1C).

Manual correction of segmentation errors is time consuming. It took  $202 \pm 26$  s per image to correct the results of the watershed algorithm. To accelerate the correction of segmentation results, we developed tools to interactively add and remove seeds before watershed segmentation. When we edited seeds, the segmentation results improved significantly, and  $94.6 \pm 0.5\%$  of cells were correctly segmented ( $P = 1.1 \times 10^{-3}$ ), with the remaining errors

corresponding to cells that were not completely within the field of view (Fig. 1B-C). Seed editing only required  $66 \pm 11$  s per image, significantly faster than polygon editing ( $P = 1.2 \times 10^{-4}$ , Fig. 1D). Our results show that seed editing is an efficient method to minimize errors in watershed-based cell segmentation.

### Seed propagation accelerates watershed segmentation

In spite of the improvement over polygon editing, a significant amount of time is necessary for seed editing in time-lapse sequences consisting of multiple images. To reduce the time necessary to segment time-lapse images, we transferred edited seeds from one time point to the next. The propagation of seeds in time also implicitly tracks the cells (Pinidiyaarachchi and Wahlby, 2005). We tested this approach by segmenting cells expressing Gap43:mCherry in *Drosophila* embryos imaged every 15 s during germband extension. Copying seeds led to segmentation errors as a consequence of cell movement (Fig. 1E and F, arrowheads). The percent of correctly segmented cells declined from  $98.8 \pm 0.9\%$  in the first time point, after seed editing, to  $42.5 \pm 2.1\%$  for images acquired 5 minutes later ( $P = 7.2 \times 10^{-9}$ , Fig. 1I). On average, apical cell areas do not change significantly during germband extension before cell division (Fernandez-Gonzalez and Zallen, 2011). The segmentation errors caused by seed copying were further demonstrated by a significant increase in the range of cell areas measured from the segmented images: the standard deviation of the distribution was  $19.1 \pm 1.6 \mu\text{m}^2$  initially (stage 7 of embryonic development) vs.  $37.0 \pm 2.2 \mu\text{m}^2$  after 5 minutes ( $P = 1.9 \times 10^{-4}$ , Fig. 1J-K). Together, our data indicate that seed copying increases the number of segmentation errors.

To compensate for cellular movements when transferring seeds across images, we used the optic flow to estimate cell displacements. We divided each pair of consecutive images into  $17.1 \times 17.1 \mu\text{m}^2$  windows (approximately  $2 \times 2$  cell diameters), and we calculated the spatial cross-correlation between the pixel values in corresponding windows. The cross-correlation maximum indicates the displacement of the signal. We obtained one vector per window, and the resulting vector field was interpolated at the positions of the seeds in the initial time point. Seeds were translated by the corresponding vector before transferring to the next time point. Using optic flow to transfer seeds led to significantly more cells correctly segmented after 5 minutes ( $89.7 \pm 4.9\%$ ,  $P = 2.1 \times 10^{-5}$ ) and a lower standard deviation of the measured areas ( $24.9 \pm 3.2 \mu\text{m}^2$ ,  $P = 1.4 \times 10^{-2}$ , Fig. 1G, I-K), demonstrating that seed propagation using optic flow preserves segmentation quality.

To further refine the segmentation results, we integrated seed detection and watershed-based expansion. The seeds for the first image were grown using the watershed algorithm. Seeds that were closer than 0.8  $\mu\text{m}$  to their enclosing, watershed-generated polygon, were translated to the geometric centre of the polygon before propagation to the next time point using optic flow (Fig. 1H, white arrows). Using this approach,  $94.9 \pm 1.6\%$  of cells were correctly segmented 5 minutes after the initial time point (Fig. 1I), and the standard deviation of the measured cell area did not increase significantly over time ( $23.6 \pm 2.5 \mu\text{m}^2$ ,  $P = 0.17$ , Fig. 1J and K). Thus, integration of watershed-based seed expansion and seed propagation using optic flow improved segmentation accuracy by over 120% with respect to seed copying, and minimized the user interactions necessary to delineate and track cells from confocal microscopy movies.

### **Cell morphology can be used to detect and track dividing cells**

During embryonic development, cells not only move, but also divide. We extended our algorithm to detect dividing cells and split their seeds before propagating to the next time point. To determine when a cell divided, we quantified changes in cell morphology (Fig. 2A) using features that ensured that cells were only classified as dividing immediately before their division was complete (Movie S1), which was critical for proper seed splitting and segmentation. We measured the maximum change in cell area as the ratio between the current area and the minimum recorded area for a cell. Dividing cells increased their apical area by  $106 \pm 15\%$  (Fig. 2B), while the maximum area increase of non-dividing cells during the same time was  $42 \pm 4\%$  ( $P = 8.6 \times 10^{-5}$ , Fig. 2E). The shape factor (Cox, 1927), proportional to the perimeter<sup>2</sup>-to-area ratio (1 for circles, greater than 1 for other shapes), decreased towards 1 as cells rounded up, and then increased rapidly when the cytokinetic furrow formed (Fig. 2C). On average the minimum recorded shape factor was  $1.30 \pm 0.01$  for dividing cells and  $1.37 \pm 0.01$  for non-dividing cells ( $P = 7.7 \times 10^{-6}$ , Fig. 2F). We quantified the characteristic dumbbell shape of dividing cells during cytokinesis by calculating the distance between the cell centroid and each point in the polygon resulting from the cell segmentation, and measuring the ratios between each of the two local distance minima (corresponding to the cleavage furrow) and the maximum (corresponding to the distance to one of the cell poles, Fig. 2D). The ratios increased towards 1 as the cells rounded up in preparation for division, and they decreased rapidly as the cleavage furrow formed (Fig. 2D'). Both ratios were significantly smaller for dividing cells with respect to non-dividing cells ( $0.36 \pm 0.01$  vs.

0.41±0.01 for the deeper end of the furrow,  $P = 5.3 \times 10^{-5}$ ; and 0.42±0.01 vs. 0.49±0.01 for the shallower end,  $P = 7.5 \times 10^{-7}$ , Fig. 2G-H). Finally, the distance between the cell centroid and the segmented polygon displayed a strong periodic pattern immediately before division, with two periods within the circumference of the cell corresponding to the two daughter cells (Fig. 2I). Thus, we used the first ten integer frequency components of the Fourier transform of the centroid-to-polygon distance as ten additional features to distinguish between dividing and non-dividing cells (Fig. 2J). For a frequency of 2, representing the presence of two peaks and two troughs in the distance plot, the magnitude of the Fourier transform was 2.2-fold greater for dividing cells ( $P = 8.4 \times 10^{-38}$ , Fig. 2J) demonstrating the presence of two clearly defined lobes before cell division.

We applied a statistical method, logistic regression, to detect dividing cells using the 14 measured features (Fig. 2E-H, J) and a training set of cells. Each cell in the training set was represented in 15-dimensional space, where 14 dimensions corresponded to the measured features, and the dependent variable was the cell classification as dividing (1) or non-dividing (0). A probability function,  $h$ , was defined by fitting a logistic function (see Materials and Methods) to the distribution of cells in 15-dimensional space. The value of  $h$  for a given set of features determines the probability that a cell with those features is dividing. Cells with a probability greater than 0.5 were considered to be dividing. We split the seed corresponding to a dividing cell into two new seeds that were placed on the longest axis of the cell, at 50% of the distance between the cell centroid and the cell boundary. To validate our approach, we determined the accuracy of classification for a test set of cells (formed by 30 dividing and 60 non-dividing cells in 7 embryos and independent from the training set) using training sets of different sizes, all with a 1:1 ratio of dividing and non-dividing cells (Fig. 2K). Using a training set including 52 cells, we correctly classified over 90% of the cells in the test set, with 2% of non-dividing cells classified as dividing (false positives). Using a training set with 80 cells, we correctly classified 97% of the test cells, with 3% false positives (Fig. 2K). Therefore, our method can efficiently detect and track dividing cells (Movie S1), thus allowing quantification of features including cell cycle duration, division orientation or morphological and molecular (a)symmetries.

To illustrate the generality of our method, we used it to segment and detect a different cell type, the ingressing neuroblasts of the early embryo. As neuroblasts ingress, their apical area decreases and their circularity increases (Movie S2, Fig. S2A). We quantified the change in



area for a cell as the ratio between the current area and the first recorded area. Neuroblasts displayed lower area change and minimum shape factor values than non-ingressing cells ( $0.23 \pm 0.02$  vs.  $1.19 \pm 0.07$  for area change,  $P = 2.2 \times 10^{-14}$ ; and  $1.21 \pm 0.01$  vs.  $1.43 \pm 0.02$  for minimum shape factor,  $P = 8.3 \times 10^{-12}$ ; Fig. S2B). Consistent with their roundness, the ratios of minimum to maximum distance from the centroid to the cell boundary were both greater for neuroblasts ( $0.48 \pm 0.02$  vs.  $0.39 \pm 0.02$  for  $min_1/max$ ,  $P = 4.1 \times 10^{-3}$ ; and  $0.55 \pm 0.02$  vs.  $0.45 \pm 0.02$  for  $min_2/max$ ,  $P = 7.3 \times 10^{-4}$ , Fig. S2C). Ingressing neuroblasts displayed lower amplitudes in the frequency components of the Fourier transform of their centroid-to-polygon distance (Fig. S2D). Using a training set formed by up to 15 neuroblasts and 15 non-ingressing cells, we correctly classified over 90% of ingressing neuroblasts in a test set formed by 15 neuroblasts and 15 non-ingressing cells in 5 embryos (Fig. S2E). Notably, removing frequency components 3-10 from the feature set resulted in 100% classification accuracy for neuroblasts and non-ingressing cells with only 12 training cells (Fig. S2E, inset). Together, these results demonstrate that given an appropriate training set, our classification framework is able to identify different cell types from confocal microscopy movies.

### **Ventral but not lateral germband cells undergo oriented cell divisions**

Mesectoderm (ventral) and lateral cells in the anterior germband divide during axis elongation (Movie S3). To investigate if the divisions of ventral and lateral cells contribute to axis elongation, we used the tools that we developed to quantify cell division orientation. We imaged stage 7-8 *Drosophila* embryos expressing Gap43:mCherry to outline cells (Fig. 3A-B). The average division orientation with respect to the AP axis for ventral cells was  $24.8 \pm 2.6^\circ$ , and the median was  $14.0^\circ$  (Fig. 3C).  $55.2 \pm 7.4\%$  of the ventral divisions occurred within  $15^\circ$  of the AP axis, and  $84.3 \pm 4.0\%$  of cells divided at less than  $45^\circ$  relative to the AP axis. To validate our automated analysis, we manually measured the angles of division for a subset of cells. We found no significant differences between automated and manual analyses (Fig. 3D). Altogether, our data indicate that ventral cells divide parallel to the AP axis of the embryo during germband extension.

Using light sheet microscopy, we found that the onset of lateral cell divisions occurred at approximately the same time as that of ventral divisions (Movie S4). In contrast to ventral cells, the distribution of division angles for lateral cells was uniform (Fig. 3B, E). The average angle of lateral cell division was  $43.4 \pm 1.7^\circ$ , significantly greater than the ventral cell division orientation ( $P = 2.2 \times 10^{-8}$ ). The median angle of lateral cell division was  $42.1^\circ$ .

18.1±3.0% of the cells divided within 15° of the AP axis, and 51.9±5.0% divided within 45° (Fig. 3E), both significantly lower percentages than for ventral cells ( $P = 1.5 \times 10^{-4}$  and  $8.0 \times 10^{-5}$ , respectively). Our results show that lateral cells do not divide directionally, suggesting that the mechanisms that orient cell division in the ventral midline are spatially regulated.

### **Ventral cells align with the AP axis in preparation for division**

Cell division angle is strongly correlated with cell shape orientation (Hertwig, 1884). To quantify cell orientation during division, we used least-squares to fit an ellipse to the polygon produced by our segmentation (Fitzgibbon et al., 1999) (Fig. 4A). We defined cell orientation as the angle of the longest axis of the ellipse relative to the AP axis. As expected, cell orientation immediately before division was closely correlated with the orientation of cell division for both ventral and lateral cells ( $r = 0.99$ ,  $P = 1.3 \times 10^{-53}$  for ventral cells;  $r = 0.98$ ,  $P = 2.4 \times 10^{-69}$  for lateral cells, Fig. 4D), thus validating our metric of cell orientation. When we examined the absolute difference between cell orientation and cell division angle, we found that between 300 s and 90 s before division, ventral cell orientation deviated more significantly from the final division angle than lateral cell orientation ( $P = 3.5 \times 10^{-4}$ , Fig. 4B-C, E). The total angular change in cell orientation, resulting from integrating the absolute value of the major cell axis rotation over the 5 minutes before division, was  $120.9^\circ \pm 9.9^\circ$  for ventral cells, significantly greater than the  $84.1^\circ \pm 4.7^\circ$  of lateral cells ( $P = 1.2 \times 10^{-3}$ , Fig. 4F). These data show that ventral cells change their alignment more significantly than lateral cells in preparation for division, suggesting that ventral cells may be responding to directional cues that determine the orientation of division.

### **Ventral cell divisions locally increase AP cell density and increase mesectoderm surface area**

Lateral germband cells intercalate and thus relieve AP strain (Collinet et al., 2015; Lye et al., 2015). Conversely, ventral cells did not intercalate during germband extension (Movie S5). As a consequence, we predicted that ventral cells sustained greater AP strain (deformation) during germband extension than lateral cells. We measured strain as the percent of change in AP or DV length between 10 and 5 minutes before the first ventral division (Fig. 5A-C). Ventral cells sustained tensile AP strain and significantly lower compressive DV strain ( $7.5 \pm 1.3\%$  vs.  $-3.3 \pm 1.9\%$ , respectively,  $P = 8.1 \times 10^{-6}$ , Fig. 5D). The AP strain sustained by ventral cells was greater than that of lateral cells ( $1.3 \pm 2.1\%$ ,  $P = 1.3 \times 10^{-2}$ ), which displayed

compressive strain along the DV axis ( $-8.2 \pm 1.9\%$ ) (Fig. 5D). Thus, 5 minutes before the onset of cell division, ventral and lateral cells sustain different types of deformation.

Oriented cell divisions could alleviate AP strain in ventral cells by reducing their AP length. Before their respective divisions, ventral cells were significantly longer along the AP axis than lateral cells ( $11.1 \pm 0.3 \mu\text{m}$  vs.  $7.8 \pm 0.4 \mu\text{m}$  600 s before division,  $P = 6.6 \times 10^{-8}$ ; and  $12.2 \pm 0.2 \mu\text{m}$  vs.  $10.0 \pm 0.2 \mu\text{m}$  300 s before division,  $P = 2.7 \times 10^{-7}$ , Fig. 5E-G). Cell division led to a significant reduction of AP length for ventral but not lateral cells ( $9.8 \pm 0.1 \mu\text{m}$  immediately after division for both ventral cells,  $P = 2.6 \times 10^{-14}$ , and lateral cells,  $P = 0.35$ , Fig. 5G). The reduction in AP length was associated with increased cell density along the AP axis. We measured cell density for both ventral and lateral cells, 5 minutes before and 12 min after division, by calculating the average number of cells intersected by three  $80 \mu\text{m}$  lines parallel to the AP axis and approximately  $7 \mu\text{m}$  (one cell diameter) apart (Fig. 5H-I). We found that ventral AP cell density increased significantly after oriented cell divisions, from  $143.3 \pm 5.4$  cells/mm to  $196.7 \pm 1.6$  cells/mm ( $P = 3.1 \times 10^{-4}$ , Fig. 5J). In contrast, lateral AP cell density did not increase after cell divisions, but rather decreased from  $252.5 \pm 5.7$  cells/mm to  $218.3 \pm 13.6$  cells/mm ( $P = 0.05$ , Fig. 5J). The lateral and ventral AP cell densities after division were not significantly different from each other ( $P = 0.19$ ). Together, our data show that ventral cells sustain greater AP strain than lateral cells during germband extension, and that oriented cell divisions selectively reduce the AP length of ventral cells, suggesting that oriented cell divisions in the mesectoderm may alleviate cell strain.

To further investigate if ventral cell divisions alleviate AP strain, we injected embryos with dsRNA against *string* (*stg*, Movie S6). String, a Cdc25 homolog (Edgar et al., 1994), is required for post-blastoderm mitoses in *Drosophila* embryos. We found that the AP length of ventral cells at the end of germband extension was significantly greater in embryos depleted of String than in controls ( $13.7 \pm 0.5 \mu\text{m}$  vs.  $8.7 \pm 0.3 \mu\text{m}$ , respectively,  $P = 6.3 \times 10^{-14}$ , Fig. 6A-C). The AP length of ventral cells in *stg* dsRNA embryos did not exceed the AP length of ventral cells before division in control embryos ( $12.9 \pm 0.4 \mu\text{m}$ , Fig. 6A-C). In controls and especially in *stg* dsRNA embryos, myosin localized to cell interfaces parallel to the AP axis within the mesectoderm and at the boundaries between mesectoderm and ectoderm (Fig. 6A'-B'), suggesting that myosin may resist excessive AP-oriented deformation.

To investigate how ventral cell divisions might contribute to axis elongation, we compared the apical area of cell duplets resulting from ventral divisions in control embryos to the maximum area of ventral cells in *stg* dsRNA embryos. The area of the duplets was significantly greater ( $83.0 \pm 3.5 \mu\text{m}^2$  vs.  $68.6 \pm 2.3 \mu\text{m}^2$  for single ventral cells in *stg* dsRNA,  $P = 9.0 \times 10^{-4}$ , Fig. 6D). Together, our results suggest that ventral divisions increase the surface area of the mesectoderm, a tissue that does not intercalate, in a process that may contribute to axis elongation.

### **Mechanical forces from the anterior and posterior poles contribute to orienting ventral cell divisions**

Mechanical forces parallel to the AP axis of the embryo contribute to germband extension (Irvine and Wieschaus, 1994; Collinet et al., 2015; Lye et al., 2015; Yu and Fernandez-Gonzalez, 2016). To investigate the role of forces in cell division alignment during *Drosophila* axis elongation, we used laser ablation to mechanically isolate ventral cells from tension generated by the internalization of the endoderm or by intercalating cells. To decouple ventral cells from the embryonic poles, we created two incisions across the ventral midline and parallel to the DV axis in stage 7 embryos, prior to the first ventral division (Fig. 7C). We quantified cell division orientation relative to the AP axis for ventral cells between the two incisions (Fig. 7D-E). In sham-irradiated controls, ventral divisions were oriented parallel to the ventral midline, with a mean angle of  $23.5 \pm 2.4^\circ$  and a median of  $15.3^\circ$ . When ventral cells were decoupled from the anterior and posterior ends of the embryo, ventral divisions displayed a mean orientation of  $39.8 \pm 4.1^\circ$ , significantly greater than in controls ( $P = 1.0 \times 10^{-3}$ ), and a median of  $30.7^\circ$ . The distribution of cell division orientations was significantly more uniform when cells were isolated from forces from the anterior and posterior ends of the embryo (Fig. 7D,  $P = 8.8 \times 10^{-3}$ ). In contrast, when we isolated ventral cells from intercalating cells by creating an incision lateral to the ventral cells and parallel to the AP axis (Fig. 7B), we found that ventral divisions were still oriented along the AP axis, with a mean angle of  $21.6 \pm 3.1^\circ$  and a median of  $18.0^\circ$  (Fig. 7D-E). Together, our data indicate that forces from the embryonic poles, but not directly transmitted from intercalating cells, orient ventral cell divisions during *Drosophila* axis elongation.

## Discussion

The mechanisms that orient cellular behaviours during embryonic development remain unclear. We introduce novel quantitative imaging tools to investigate the orientation and dynamics of cell division. We find that ventral but not lateral germband cells undergo oriented cell divisions during axis elongation. Oriented cell divisions increase cell density parallel to the AP axis of the embryo, alleviate AP strain, and may facilitate tissue elongation by increasing the surface area of the mesectoderm. Using laser ablation, we find that isolating ventral cells from the anterior and posterior ends of the embryo significantly alters the orientation of divisions, suggesting that tissue-wide forces determine cell division orientation during *Drosophila* axis elongation.

To investigate oriented cell divisions during germband extension, we have developed image-based cell segmentation and classification tools based on the watershed algorithm. Our method provides several advantages over previous approaches. First, we allow the user to correct seeds, instead of polygons, which minimizes user interactions (Mashburn et al., 2012). Second, corrected seeds can be transferred to other images in time-lapse sequences while taking cell movements into account by using optical flow and integrating seed propagation with cell segmentation. Thus, seeds need only be edited in one image, further reducing user intervention. Third, we apply a statistical method, logistic regression, to determine the probability that a cell is dividing based on cell morphology. Using logistic regression and a relatively modest training set of 52 cells, we correctly classify over 90% of cells in a test set, with a false positive rate of only 2%. We provide interactive tools to correct the results of logistic regression, and we use the corrections to further train our algorithm, thus seamlessly integrating user knowledge into our automated classification scheme. Importantly, the use of machine learning confers generality to our approach, as creating different training sets allows application of the same method to other cell types, tissues and/or fluorescent markers.

Our data suggest that mechanical cues orient cell division during germband extension. Endoderm internalization on the posterior end of the embryo imposes AP-oriented tension on the germband (Collinet et al., 2015; Lye et al., 2015) that could orient cell divisions. It has been proposed that segmental patterning orients cell division in the posterior germband (da Silva and Vincent, 2007). In embryos maternally triple mutant for *bicoid*, *nanos* and *torso*-

*like*, which completely lack AP-patterning, all posterior divisions during germband extension are randomly oriented (da Silva and Vincent, 2007). However, *torso-like* is necessary for endoderm invagination (Degelmann et al., 1986), and therefore, the orientation of posterior-ventral divisions may be regulated by global mechanical cues generated as the endoderm is internalized.

We find that on the anterior end of the germband, ventral, but not lateral cells, undergo oriented division. The curvature of the *Drosophila* embryo is greater on the ventral than on the dorsal or lateral surfaces (He et al., 2010). Thus, as the endoderm is internalized and the germband elongates, ventral cells need to cover a greater surface area than lateral cells. In addition, lateral cells intercalate during axis elongation, thus increasing cell density along the AP axis and partially relieving the tension caused by the internalization of the endoderm (Collinet et al., 2015; Lye et al., 2015). In contrast, ventral cells do not intercalate, and they sustain increased AP strain with respect to lateral cells before the onset of division. Together, our data support a model in which ventral cells divide directionally to alleviate the tension caused by endoderm invagination, increased ventral curvature and the absence of intercalary behaviours.

The mechanisms by which physical forces orient cell division during *Drosophila* axis elongation remain unclear. In *Drosophila* neuroblasts, the asymmetric localization of the polarity factor Par-3 determines the direction of division (Schober et al., 1999; Wodarz et al., 1999). Par-3 is planar-polarized in lateral germband cells (Zallen and Wieschaus, 2004; Blankenship et al., 2006), which do not display a bias in the directionality of their division, suggesting that Par-3 may not be involved in cell division orientation during germband extension. Par-3 regulates cell division orientation by recruiting the G-protein regulator Pins (Schober et al., 1999; Wodarz et al., 1999; Yu et al., 2000; Schaefer et al., 2001) and the Pins-binding protein Mud (Bowman et al., 2006; Izumi et al., 2006; Siller et al., 2006), which form a complex that interacts with the microtubule-based motor Dynein and facilitates spindle orientation (Merdes et al., 1996). Recent data show that in the dorsal thorax of the *Drosophila* pupa, Mud localizes to tricellular junctions independently of Pins, and regulates the pulling forces that astral microtubules exert on centrosomes (Bosveld et al., 2016). Thus, the distribution of tricellular junctions around a dividing cell determines centrosome position, spindle alignment and cell division orientation. Investigating the distribution of tricellular junctions around ventral cells, and how the different cell behaviours and forces at play in the

germband affect tricellular junctions may therefore be critical to understand how mechanical forces direct cell division orientation during *Drosophila* axis elongation.

## Materials and Methods

### Fly stocks

For live imaging we used stage 7-8 embryos expressing *sqh-gap43:mCherry* (Martin et al., 2010) and *sqh-sqh:GFP* (Royou et al., 2004).

### Time-lapse imaging

*Drosophila* embryos were dechorionated for 2 minutes using a 50% bleach solution in water. Embryos were mounted in halocarbon oil 27 between an 18x18 mm coverglass and an oxygen-permeable membrane (YSI). Embryos were imaged using a Revolution XD spinning disk confocal microscope with an iXon Ultra 897 camera (Andor) and either a 40x (NA 1.35) or 60x (NA 1.35) oil-immersion lens (Olympus). Z-stacks consisting of 14 slices 0.3  $\mu\text{m}$  apart were acquired every 15 s at 16 bits. 1-4 slices were projected per stack.

For light-sheet microscopy, embryos were mounted in warm 2% agar inside of a glass capillary and the agar was allowed to set. Embryos were extruded from the capillary and mounted in the water-filled chamber of the light-sheet microscope. Dual-sided light-sheet excitation was provided by two 20x long-working distance air objectives (Olympus), and emission was imaged through a 20x (NA 0.5) water-immersion objective (Olympus). Ventral and lateral Z-stacks consisting of 14 slices 3  $\mu\text{m}$  apart were acquired every 25 seconds using a Neo sCMOS camera (Andor). 3 slices were projected per stack.

### Automated delineation and tracking of dividing cells

To delineate and track dividing cells from fluorescence microscopy movies, we developed a new method based on the watershed algorithm for cell segmentation, optic flow for seed propagation, and machine learning for division detection. Our method was implemented using Matlab (Mathworks) and the DIPImage toolbox (TU Delft, The Netherlands), and integrated into SIESTA (Fernandez-Gonzalez and Zallen, 2011), an image analysis platform that we develop and can be downloaded from <http://individual.utoronto.ca/quantmorph/software.html>.



## Watershed segmentation

The watershed algorithm is a region-growing segmentation method based on the identification and expansion of one seed point per cell (Beucher, 1992). We identified seeds exclusively for the first time point of an image sequence using an adaptive threshold (Fernandez-Gonzalez and Zallen, 2011). Seeds were edited using interactive tools provided by SIESTA (Leung and Fernandez-Gonzalez, 2015). Seeds were then propagated to subsequent time points in the image sequence using optic flow.

## Seed propagation

The optic flow is a vector field that quantifies local signal displacements across two images. To propagate watershed seeds, we took pixels (one in every 32) with corresponding coordinates in the source and target images, and defined a 64x64 pixel window (approximately two cell diameters) around each pixel. We calculated the cross-correlation of the pixel values for corresponding windows in the source and target images. The maxima of the cross-correlation indicate the coordinates of a vector representing the signal displacement. The vector field was bilinearly interpolated at the positions of the seeds on the source image to obtain the optic flow at the seed points. Seeds were translated by the magnitude and direction of the corresponding vectors before transferring to the target image.

In embryos, cells do not only experience translations, but also deformations. Therefore, optic flow alone did not always successfully propagate seeds. To address this issue, we integrated seed propagation and cell segmentation. After propagating the seeds to the next time point, the watershed algorithm was used to detect cell outlines. Seeds that were within 3 pixels from the cell boundary were shifted to the cell centroid before propagating to the next time point. Cell tracking was implicitly done by the seed propagation algorithm except in the case of dividing cells.

## Detection of dividing cells

We employed a logistic regression algorithm to identify dividing and non-dividing cells. At every time point in which a cell was segmented, we measured 14 features that described the morphology of the cell (Fig. 2E-H, J). We quantified the area increase ratio, defined as the ratio between the current cell area and the minimum recorded cell area including its present value. We also calculated the shape factor, a measurement of circularity defined as:



$$\text{shape factor} = \frac{p^2}{4\pi a} \quad (\text{Equation 1}),$$

where  $p$  and  $a$  are the apical cell perimeter and area, respectively. To measure the characteristic dumbbell shape of dividing cells during cytokinesis, we quantified the distance between the cell centroid and all the pixels on the polygon resulting from the segmentation. We stored the ratios between each of the two local minima of the centroid-polygon distance to the absolute maximum. Finally, we stored the magnitudes of the 1-10 integer frequency components of the Fourier transform of the centroid-polygon distance curve (features 5-14).

We employed logistic regression, a machine learning technique (Bishop, 2006), to determine if cells were dividing or not based on the 14 features that we measured. Cells were represented in  $(m+1)$ -dimensional space, where  $m = 14$  features, and the additional dimension is 1 if the cell is dividing, or 0 if it is not. We fitted a logistic function,  $h$ , to the distribution of a training set consisting of dividing and non-dividing cells. For a given feature set,  $\mathbf{x}$ ,  $h(\mathbf{x})$  represented the probability of a cell to be dividing:

$$h_{\theta}(\mathbf{x}) = \frac{1}{1+e^{-\theta\mathbf{x}}} \quad (\text{Equation 2}),$$

where  $\theta$  is a vector of scaling parameters used to fit the training set distribution. To find the value of  $\theta$  that resulted in the optimal discrimination between dividing and non-dividing cells, we minimized a cost function,  $J$ :

$$J(\theta) = \frac{1}{m} \sum_{i=1}^m [-y_i \log(h_{\theta}(\mathbf{x}_i)) - (1 - y_i) \log(1 - h_{\theta}(\mathbf{x}_i))] \quad (\text{Equation 3}),$$

where  $m$  is the number of cells in the training set,  $y_i$  is the classification of the  $i$ th training example (1 for dividing cells, 0 for non-dividing cells), and  $\mathbf{x}_i$  is a vector of measurements corresponding to the  $i$ th training example. Users could define new training examples by annotating correctly or incorrectly classified cells. With each new training example, a new optimal  $\theta$  was calculated. Cells with  $h \geq 0.5$  were considered to be dividing, while cells with  $h < 0.5$  were considered non-dividing. To improve classification accuracy, we ensured that cells identified as dividing were tracked for at least 2.5 min prior to division, displayed an apical area greater than the mean cell area at the time of division, and had a minimum-to-

maximum centroid-to-polygon distance ratio smaller than 0.45. When a cell was identified as dividing, its seed was split into two new seeds placed on the longest axis of the cell, at 50% of the distance between the cell centroid and the cell boundary.

### Image quantification

Images were rotated so that the ventral midline of the embryo was parallel to the horizontal axis. The percent of cells correctly segmented was calculated by counting the number of cells correctly outlined and dividing by the total number of polygons resulting from the segmentation. The orientation of cell division was measured in the first time point in which the seeds were split, as the angle between a line connecting the centroids of the two daughter cells and the horizontal axis of the image. AP or DV cell length were measured as the width or the height, respectively, of a bounding box containing the cell, effectively representing the length of the cell projected on the AP or DV axis.

### dsRNA injections

The *stg* dsRNA template was amplified by PCR from genomic DNA, using the following primer pairs with the T7 promoter sequence (5'-TAATACGACTCACTATAGGGAGACCAC-3') added to the 5' ends:

*stg* T7-forward, 5' CGGCTACAAGGAGTTCTTCG 3';

*stg* T7-reverse, 5' CGTCGTGTGCGAGAACTTA 3'.

We generated dsRNA from the PCR products using the MEGAscript T7 Transcription Kit (Fisher).

*sqh-gap43:mCherry;sqh-sqh:GFP* embryos collected for 50-60 min were dechorionated, glued on a glass cover slip, dehydrated for 10-15 minutes, and covered in halocarbon oil 27 (Sigma-Aldrich). Embryos were immediately injected laterally with 1.86 µg/µL of dsRNA against *stg* using a Transferrman NK2 micromanipulator (Eppendorf) and a PV820 microinjector (WPI). Control embryos were injected with water. Embryos were incubated in a humidified chamber for 2 hours at room temperature after injection. Z-stacks consisting of 10 slices 0.3 µm apart were acquired every 30 s at 16 bits. 1-4 slices were projected per stack.

## Laser ablation

To mechanically isolate cells from AP-oriented forces, we used a pulsed Micropoint N<sub>2</sub> laser (Andor) tuned to 365 nm to cut lines on the germband. The laser delivered 2-6 ns pulses at a power of 120  $\mu$ J per pulse at the source. We induced line wounds by a series of discrete point ablations  $\sim 1.7$   $\mu$ m apart. 3-5 laser pulses were delivered to each point. DV lines had 50-60  $\mu$ m in length and were 80-90  $\mu$ m apart along the AP axis. AP lines were 50-60  $\mu$ m and were at least two cell layers away from the ventral midline. Line ablations were done before completion of the first ventral division. For control experiments, the laser was fully attenuated using a neutral density filter.

## Statistical analysis

We compared sample variances using the *F*-test. We used Student's *t*-test modified for samples with equal or unequal variances (based on the *F*-test results) to compare sample means. When three or more samples were considered, we applied Holm's correction to Student's *t*-test (Glantz, 2002). We used the Kolmogorov-Smirnov test to compare sample distributions. We calculated the significance of correlation coefficients by transforming the correlation value into a *t*-statistic using the *corrcoef* Matlab function (Mathworks). Error bars represent the standard error of the mean (s.e.m.) unless otherwise indicated.

## **Acknowledgements**

We are grateful to Anna Kobb, Teresa Zulueta-Coarasa, Jessica Yu and Hester van Dorst for comments on the manuscript; and to Ulli Tepass and Penney Gilbert for useful discussions. Flybase provided important information for this study. The authors declare no competing financial interests.

## **Author contributions**

M.F.Z.W. and R.F.G. conceived the project. M.F.Z.W., G.W., C.M., C.M.Y. and R.F.G. developed tools. M.F.Z.W., M.V.H., G.W. and C.M. conducted the experiments. M.F.Z.W., and R.F.G. analyzed the data and prepared the manuscript. All authors edited the manuscript prior to submission.

## References

- Aigouy, B., Farhadifar, R., Staple, D. B., Sagner, A., Roper, J. C., Julicher, F. and Eaton, S.** (2010). Cell flow reorients the axis of planar polarity in the wing epithelium of *Drosophila*. *Cell* **142**, 773-786.
- Bertet, C., Sulak, L. and Lecuit, T.** (2004). Myosin-dependent junction remodelling controls planar cell intercalation and axis elongation. *Nature* **429**, 667-671.
- Beucher, S.** (1992). The watershed transformation applied to image segmentation. *Scanning Microsc. Suppl.* **6**, 299-314.
- Bishop, C. M.** (2006). *Pattern recognition and machine learning*. New York: Springer.
- Blankenship, J. T., Backovic, S. T., Sanny, J. S., Weitz, O. and Zallen, J. A.** (2006). Multicellular rosette formation links planar cell polarity to tissue morphogenesis. *Dev. Cell* **11**, 459-470.
- Bosveld, F., Markova, O., Guirao, B., Martin, C., Wang, Z., Pierre, A., Balakireva, M., Gague, I., Ainslie, A., Christophorou, N., et al.** (2016). Epithelial tricellular junctions act as interphase cell shape sensors to orient mitosis. *Nature* **530**, 495-498.
- Bowman, S. K., Neumuller, R. A., Novatchkova, M., Du, Q. and Knoblich, J. A.** (2006). The *Drosophila* NuMA Homolog Mud regulates spindle orientation in asymmetric cell division. *Dev. Cell* **10**, 731-742.
- Butler, L. C., Blanchard, G. B., Kabla, A. J., Lawrence, N. J., Welchman, D. P., Mahadevan, L., Adams, R. J. and Sanson, B.** (2009). Cell shape changes indicate a role for extrinsic tensile forces in *Drosophila* germ-band extension. *Nat. Cell Biol.* **11**, 859-864.
- Campinho, P., Behrndt, M., Ranft, J., Risler, T., Minc, N. and Heisenberg, C. P.** (2013). Tension-oriented cell divisions limit anisotropic tissue tension in epithelial spreading during zebrafish epiboly. *Nat. Cell Biol.* **15**, 1405-1414.
- Collinet, C., Rauzi, M., Lenne, P. F. and Lecuit, T.** (2015). Local and tissue-scale forces drive oriented junction growth during tissue extension. *Nat. Cell Biol.* **17**, 1247-1258.
- Cox, E. P.** (1927). A method of assigning numerical and percentage values to the degree of roundness of sand grains. *J. Paleontol.* **1**, 179-183.
- da Silva, S. M. and Vincent, J.-P.** (2007). Oriented cell divisions in the extending germband of *Drosophila*. *Development* **134**, 3049-3054.
- Degelmann, A., Hardy, P. A., Perrimon, N. and Mahowald, A. P.** (1986). Developmental analysis of the torso-like phenotype in *Drosophila* produced by a maternal-effect locus. *Dev. Biol.* **115**, 479-489.
- Edgar, B. A., Lehman, D. A. and O'Farrell, P. H.** (1994). Transcriptional regulation of string (*cdc25*): a link between developmental programming and the cell cycle. *Development* **120**, 3131-3143.
- Etournay, R., Merkel, M., Popovic, M., Brandl, H., Dye, N. A., Aigouy, B., Salbreux, G., Eaton, S. and Julicher, F.** (2016). TissueMiner: A multiscale analysis toolkit to quantify how cellular processes create tissue dynamics. *eLife* **5**.
- Fernandez-Gonzalez, R., Simoes Sde, M., Roper, J. C., Eaton, S. and Zallen, J. A.** (2009). Myosin II dynamics are regulated by tension in intercalating cells. *Dev. Cell* **17**, 736-743.
- Fernandez-Gonzalez, R. and Zallen, J. A.** (2011). Oscillatory behaviors and hierarchical assembly of contractile structures in intercalating cells. *Phys. Biol.* **8**, 045005.
- Fitzgibbon, A., Pilu, M. and Fisher, R. B.** (1999). Direct least square fitting of ellipses. *IEEE Trans. Pattern Anal. Mach. Intell.* **21**, 476-480.

- Foe, V. E.** (1989). Mitotic domains reveal early commitment of cells in *Drosophila* embryos. *Development* **107**, 1-22.
- Gillies, T. E. and Cabernard, C.** (2011). Cell division orientation in animals. *Curr. Biol.* **21**, R599-609.
- Glantz, S. A.** (2002). *Primer of biostatistics* (5th edn). New York: McGraw-Hill, Medical Pub. Div.
- Guirao, B., Rigaud, S. U., Bosveld, F., Bailles, A., Lopez-Gay, J., Ishihara, S., Sugimura, K., Graner, F. and Bellaiche, Y.** (2015). Unified quantitative characterization of epithelial tissue development. *eLife* **4**.
- Hartenstein, V. and Campos-Ortega, J. A.** (1985). Fate-mapping in wild-type *Drosophila melanogaster*. *Wilhelm Roux Arch. Dev. Biol.* **194**, 181-195.
- He, F., Wen, Y., Cheung, D., Deng, J., Lu, L. J., Jiao, R. and Ma, J.** (2010). Distance measurements via the morphogen gradient of Bicoid in *Drosophila* embryos. *BMC Dev. Biol.* **10**, 80.
- Hertwig, O.** (1884). *Das Problem der Befruchtung und der Isotropie des Eies. Eine Theorie der Vererbung*. Jenaische Zeitschrift für Naturwissenschaft.
- Irvine, K. D. and Wieschaus, E.** (1994). Cell intercalation during *Drosophila* germband extension and its regulation by pair-rule segmentation genes. *Development* **120**, 827-841.
- Izumi, Y., Ohta, N., Hisata, K., Raabe, T. and Matsuzaki, F.** (2006). *Drosophila* Pins-binding protein Mud regulates spindle-polarity coupling and centrosome organization. *Nat. Cell Biol.* **8**, 586-593.
- Jacobs, J. R. and Goodman, C. S.** (1989). Embryonic development of axon pathways in the *Drosophila* CNS. I. A glial scaffold appears before the first growth cones. *J. Neurosci.* **9**, 2402-2411.
- Jones, T. R., Carpenter, A. E., Lamprecht, M. R., Moffat, J., Silver, S. J., Grenier, J. K., Castoreno, A. B., Eggert, U. S., Root, D. E., Golland, P., et al.** (2009). Scoring diverse cellular morphologies in image-based screens with iterative feedback and machine learning. *Proc. Natl. Acad. Sci. U. S. A.* **106**, 1826-1831.
- Klamt, C., Jacobs, J. R. and Goodman, C. S.** (1991). The midline of the *Drosophila* central nervous system: a model for the genetic analysis of cell fate, cell migration, and growth cone guidance. *Cell* **64**, 801-815.
- Le Goff, L. and Lecuit, T.** (2011). Developmental biology. Gradient scaling and growth. *Science* **331**, 1141-1142.
- Leung, C. Y. B. and Fernandez-Gonzalez, R.** (2015). Quantitative image analysis of cell behavior and molecular dynamics during tissue morphogenesis. *Methods Mol. Biol.* **1189**, 99-113.
- Lye, C. M., Blanchard, G. B., Naylor, H. W., Muresan, L., Huisken, J., Adams, R. J. and Sanson, B.** (2015). Mechanical Coupling between Endoderm Invagination and Axis Extension in *Drosophila*. *PLoS Biol.* **13**, e1002292.
- Mao, Y., Tournier, A. L., Bates, P. A., Gale, J. E., Tapon, N. and Thompson, B. J.** (2011). Planar polarization of the atypical myosin Dachs orients cell divisions in *Drosophila*. *Genes Dev.* **25**, 131-136.
- Mao, Y., Tournier, A. L., Hoppe, A., Kester, L., Thompson, B. J. and Tapon, N.** (2013). Differential proliferation rates generate patterns of mechanical tension that orient tissue growth. *EMBO J.* **32**, 2790-2803.
- Martin, A. C., Gelbart, M., Fernandez-Gonzalez, R., Kaschube, M. and Wieschaus, E. F.** (2010). Integration of contractile forces during tissue invagination. *J. Cell Biol.* **188**, 735-749.

- Mashburn, D. N., Lynch, H. E., Ma, X. and Hutson, M. S.** (2012). Enabling user-guided segmentation and tracking of surface-labeled cells in time-lapse image sets of living tissues. *Cytometry A* **81**, 409-418.
- Merdes, A., Ramyar, K., Vechio, J. D. and Cleveland, D. W.** (1996). A complex of NuMA and cytoplasmic dynein is essential for mitotic spindle assembly. *Cell* **87**, 447-458.
- Mosaliganti, K. R., Noche, R. R., Xiong, F., Swinburne, I. A. and Megason, S. G.** (2012). ACME: automated cell morphology extractor for comprehensive reconstruction of cell membranes. *PLoS Comput. Biol.* **8**, e1002780.
- Pare, A. C., Vichas, A., Fincher, C. T., Mirman, Z., Farrell, D. L., Mainieri, A. and Zallen, J. A.** (2014). A positional Toll receptor code directs convergent extension in *Drosophila*. *Nature* **515**, 523-527.
- Paszek, M. J., Zahir, N., Johnson, K. R., Lakins, J. N., Rozenberg, G. I., Gefen, A., Reinhart-King, C. A., Margulies, S. S., Dembo, M., Boettiger, D., et al.** (2005). Tensional homeostasis and the malignant phenotype. *Cancer Cell* **8**, 241-254.
- Pinidiyaarachchi, A. and Wahlby, C.** (2005). Seeded watersheds for combined segmentation and tracking of cells. *Lect Notes Comput Sc* **3617**, 336-343.
- Raffel, M., Willert, C. E. and Kompenhans, J.** (1998). *Particle Image Velocimetry: A Practical Guide*. Berlin; New York: Springer.
- Rauzi, M., Verant, P., Lecuit, T. and Lenne, P. F.** (2008). Nature and anisotropy of cortical forces orienting *Drosophila* tissue morphogenesis. *Nat. Cell Biol.* **10**, 1401-1410.
- Royou, A., Field, C., Sisson, J. C., Sullivan, W. and Karess, R.** (2004). Reassessing the role and dynamics of nonmuscle myosin II during furrow formation in early *Drosophila* embryos. *Mol. Biol. Cell* **15**, 838-850.
- Sawyer, J. K., Choi, W., Jung, K. C., He, L., Harris, N. J. and Peifer, M.** (2011). A contractile actomyosin network linked to adherens junctions by Canoe/afadin helps drive convergent extension. *Mol. Biol. Cell* **22**, 2491-2508.
- Schaefer, M., Petronczki, M., Dorner, D., Forte, M. and Knoblich, J. A.** (2001). Heterotrimeric G proteins direct two modes of asymmetric cell division in the *Drosophila* nervous system. *Cell* **107**, 183-194.
- Schiegg, M., Hanslovsky, P., Haubold, C., Koethe, U., Hufnagel, L. and Hamprecht, F. A.** (2015). Graphical model for joint segmentation and tracking of multiple dividing cells. *Bioinformatics* **31**, 948-956.
- Schober, M., Schaefer, M. and Knoblich, J. A.** (1999). Bazooka recruits Inscuteable to orient asymmetric cell divisions in *Drosophila* neuroblasts. *Nature* **402**, 548-551.
- Siller, K. H., Cabernard, C. and Doe, C. Q.** (2006). The NuMA-related Mud protein binds Pins and regulates spindle orientation in *Drosophila* neuroblasts. *Nat. Cell Biol.* **8**, 594-600.
- Siller, K. H. and Doe, C. Q.** (2009). Spindle orientation during asymmetric cell division. *Nat. Cell Biol.* **11**, 365-374.
- Simões, S., Blankenship, J. T., Weitz, O., Farrell, D. L., Tamada, M., Fernandez-Gonzalez, R. and Zallen, J. A.** (2010). Rho-kinase directs Bazooka/Par-3 planar polarity during *Drosophila* axis elongation. *Dev. Cell* **19**, 377-388.
- Van Valen, D. A., Kudo, T., Lane, K. M., Macklin, D. N., Quach, N. T., DeFelice, M. M., Maayan, I., Tanouchi, Y., Ashley, E. A. and Covert, M. W.** (2016). Deep Learning Automates the Quantitative Analysis of Individual Cells in Live-Cell Imaging Experiments. *PLoS Comput. Biol.* **12**, e1005177.
- Wahlby, C., Sintorn, I. M., Erlandsson, F., Borgefors, G. and Bengtsson, E.** (2004). Combining intensity, edge and shape information for 2D and 3D segmentation of cell nuclei in tissue sections. *J. Microsc.* **215**, 67-76.

- Wodarz, A., Ramrath, A., Kuchinke, U. and Knust, E.** (1999). Bazooka provides an apical cue for Inscuteable localization in *Drosophila* neuroblasts. *Nature* **402**, 544-547.
- Yu, F., Morin, X., Cai, Y., Yang, X. and Chia, W.** (2000). Analysis of partner of inscuteable, a novel player of *Drosophila* asymmetric divisions, reveals two distinct steps in inscuteable apical localization. *Cell* **100**, 399-409.
- Yu, J. C. and Fernandez-Gonzalez, R.** (2016). Local mechanical forces promote polarized junctional assembly and axis elongation in *Drosophila*. *eLife* **5**.
- Zallen, J. A. and Wieschaus, E.** (2004). Patterned gene expression directs bipolar planar polarity in *Drosophila*. *Dev. Cell* **6**, 343-355.



## Development • Advance article

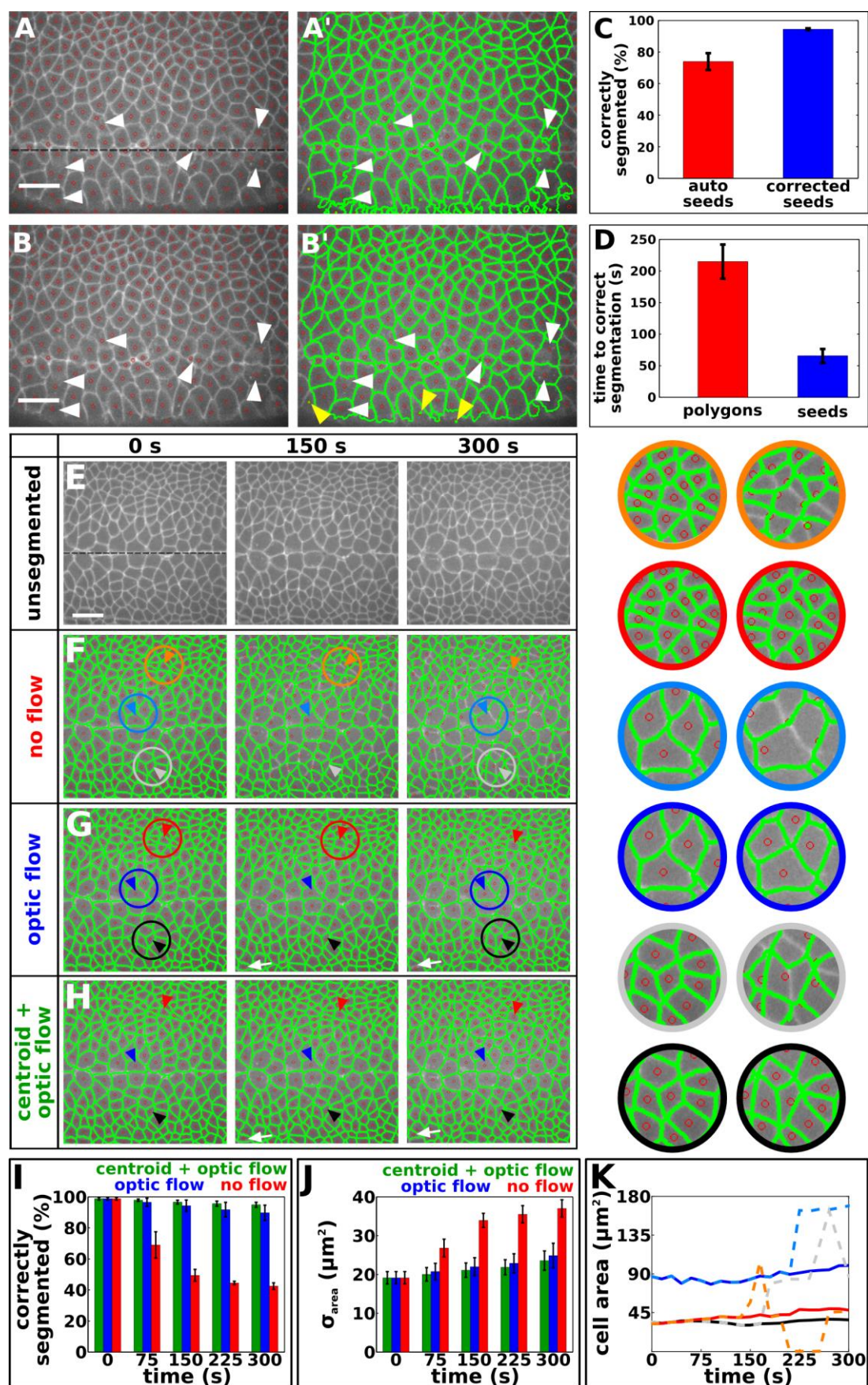


**Figure 1. Watershed-based segmentation and optic flow enable automated cell tracking over time.** (A-B) Germband cells in a stage 7 embryo expressing Gap43:mCherry. Anterior left, ventral midline across the centre (dashed line in A). Seeds (red circles) and watershed segmentation (green polygons) resulting from adaptive thresholding and distance transform with no corrections (A) or after interactive seed editing (B). Bars, 20  $\mu$ m. White arrowheads indicate errors in seed detection and subsequent segmentation errors (A) or corrected seeds and resulting segmented cells (B). Yellow arrowheads denote incorrect segmentation results in cells only partially within the field of view. (C) Percent of correctly segmented cells when seeds were not edited (red) or when they were edited (blue). (D) Time necessary to correct the segmentation results by editing polygons (red) or seeds (blue). (C-D) 3,629 cells were segmented in  $n = 10$  images from 10 different embryos. (E) Ventral germband cells expressing Gap43:mCherry at different time points with respect to the onset of cell division during axis elongation, which occurred at 375 s. Bar, 20  $\mu$ m. Anterior left, ventral midline across the centre (dashed line). (F-H) Segmentation of the images in (E) based on the seeds at  $t = 0$  s, directly copied over time (F), using optic flow to correct the position of the seeds (G), or using seed centering and optic flow (H). Arrowheads indicate cells whose areas were tracked in (K). Examples are magnified on the right. White arrows track a cell that requires seed centering for proper segmentation. (I-J) Percent of correctly segmented cells (I) and standard deviation of the measured cell areas (J) when seeds are copied across time points (red), or transferred using optic flow (blue) or seed centering and optic flow (green). 1,210 cells were segmented, tracked and measured in  $n = 5$  embryos, for a total of 6,050 delineated cells. (K) Area of three cells indicated by arrowheads in (F-H). Line and arrowhead colours correspond, continuous lines indicate the use of optical flow to propagate seeds in time, dashed lines show the results using seed copying. (C-D, I-J) Error bars, s.e.m.

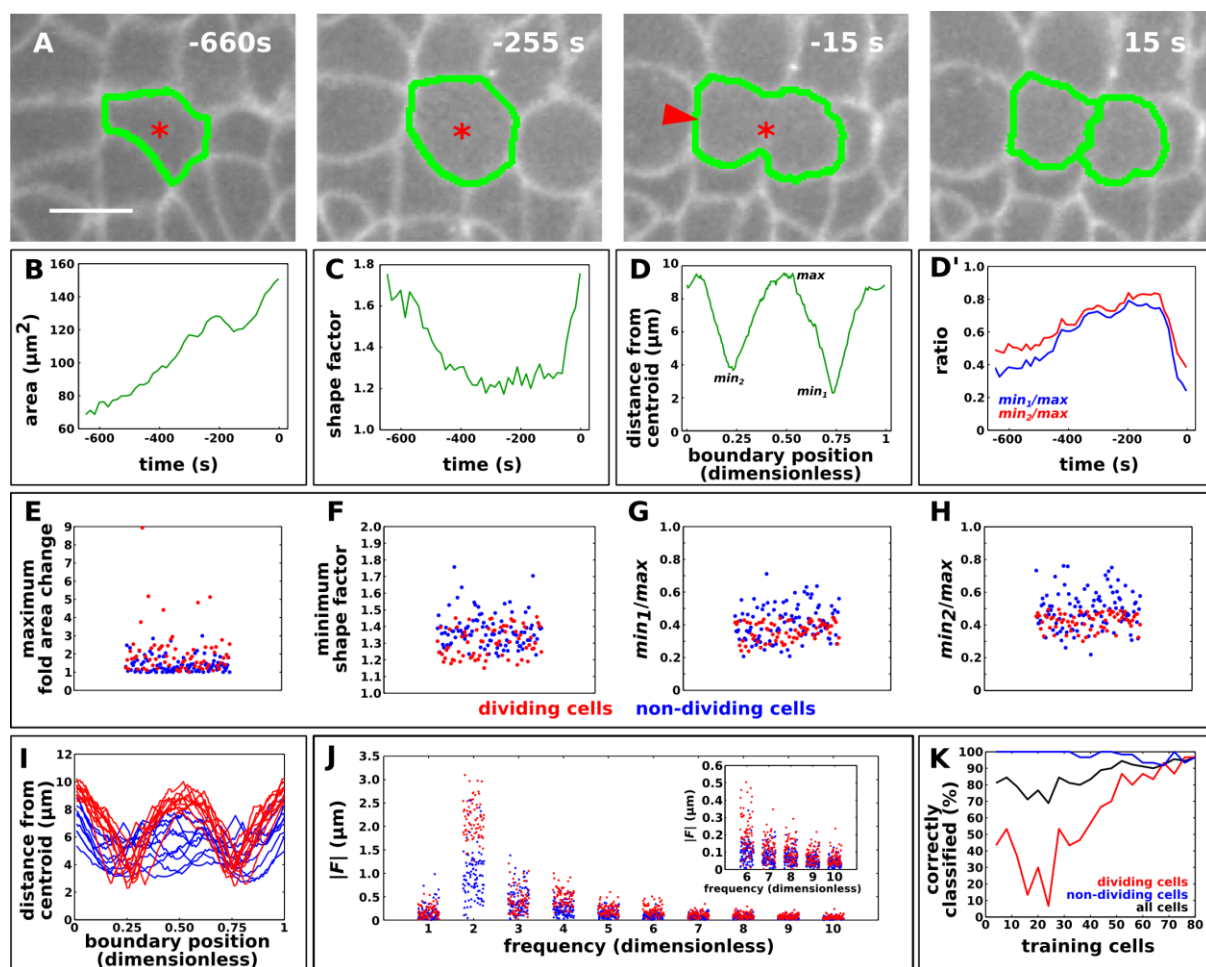


**Fig. 2. Dividing cells display distinct morphological features.** (A) Dividing germband cells expressing Gap43:mCherry. Green shows segmentation result, red asterisks indicate the cell centroid. Bar, 10  $\mu\text{m}$ . Anterior left, ventral down. Time is with respect to the time of cell division. Arrowhead indicates initial position for (D). For demonstrative purposes, the same cell is shown in Fig 4A. (B-C) Cell area (B) and shape factor (C) over time for the cell in (A). (D) Distance from the cell centroid to all the pixels along the cell boundary polygon for the cell in (A) 15 s before cell division. Pixel positions are parameterized with respect to the arrowhead in A, clockwise. (D') Temporal changes in the ratios  $\text{min}_1/\text{max}$  (blue) and  $\text{min}_2/\text{max}$  (red). (E-H,J) Scatter plots of the maximum area increase ratio (E), minimum shape factor (F), minimum-to-maximum cell radii ratios (G-H), and 1-10 integer components of the Fourier transform of the centroid-polygon distance (J) both for dividing cells ( $n=70$  in 7 embryos, red) and non-dividing cells ( $n=100$  in 5 embryos, blue). (J) Inset shows the magnitude of frequency components 6-10 with a different Y-axis scale. (I) Centroid-polygon distance for 10 dividing cells (red) and 10 non-dividing cells (blue). (I-J) Measurements were done 15 s before division was complete or when a non-dividing cell had been tracked for at

least 2 min. (K) Percent correctly classified dividing (red), non-dividing (blue), and total (black) cells based on the number of cells in the training set.



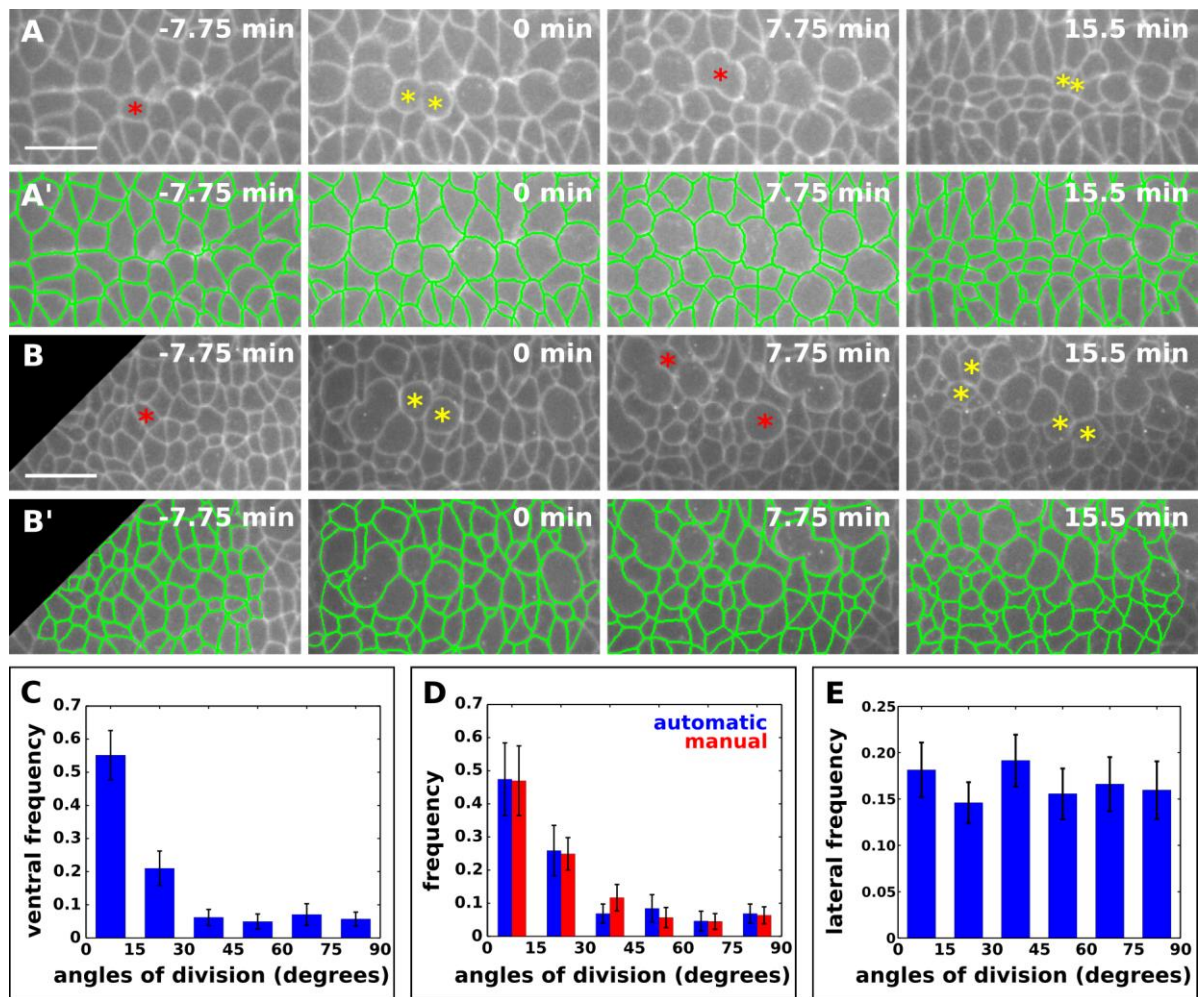


**Figure 3. Ventral cell divisions in the germband are oriented parallel to the AP axis. (A-B)** Ventral (A) and lateral (B) cells expressing Gap43:mCherry in embryos during the final stages of germband extension. Bar, 20  $\mu$ m. Time is with respect to the first ventral (A) or lateral (B) cell division. Red asterisks highlight parent cells, yellow asterisks indicate the two resulting daughter cells. **(A'-B')** Segmentation results for the images in (A-B). **(C, E)** Quantification of ventral (C) or lateral (E) cell division orientations relative to the ventral midline using automated cell segmentation and tracking (87 divisions in  $n = 17$  embryos in C; 241 divisions in  $n = 15$  embryos in E). **(D)** Quantification of ventral cell division orientations for a subset of 53 divisions in  $n = 8$  embryos using automated cell segmentation (blue) or manual measurements (red). **(C-E)** Error bars, s.e.m.

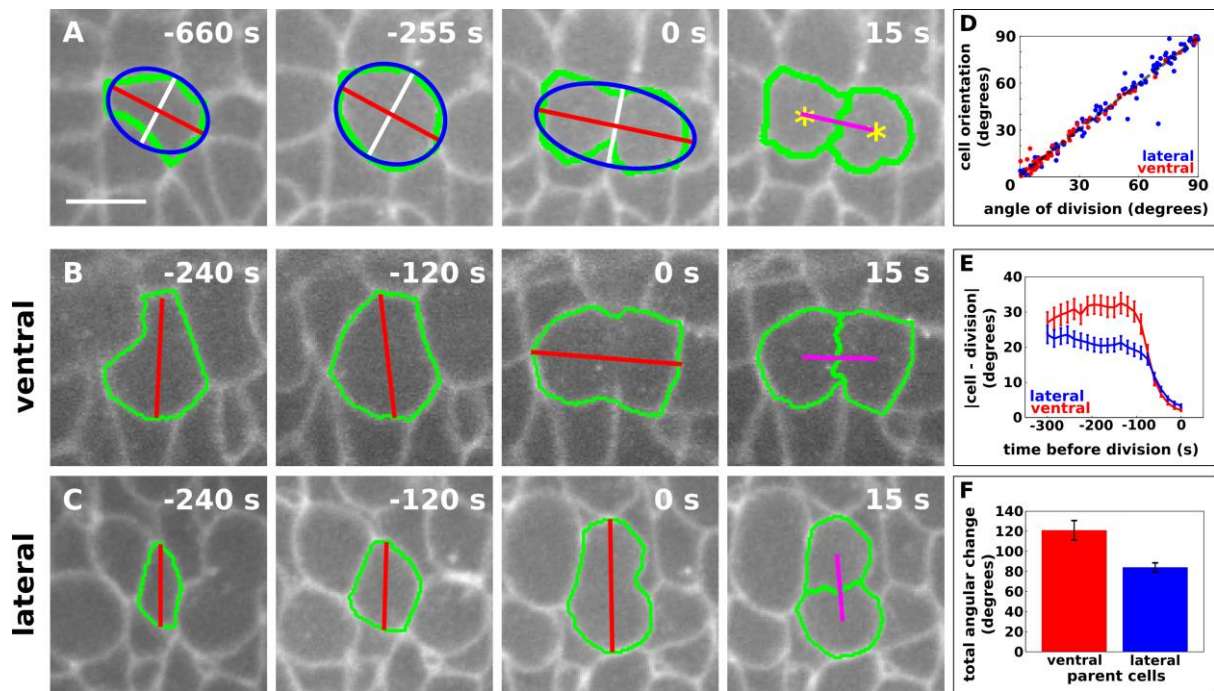


**Fig. 4. Ventral cells change their orientation significantly to align with the AP axis. (A-C)**

Cells expressing Gap43:mCherry in an embryo undergoing germband extension. Green shows segmentation results. Time is relative to the time point immediately before division. Bar, 10  $\mu$ m. Anterior left, ventral down. (A) Quantification of cell orientation and division angle from segmentation results for the cell shown in Fig. 2A. Blue indicates the least-squares ellipse fit, and red and white depict the long and short axes of the ellipse, respectively. Yellow asterisks represent the cell centroids after division and magenta indicates the axis of division. (B-C) Ventral (B) and lateral (C) cells. Red indicates the long cell axis, magenta shows the angle of division. (D-F) Cell division angle versus cell orientation immediately before the end of division (D), difference between cell orientation and cell division angle over time (E), and total absolute angular change in cell orientation from 300 s to 0 s before division (F) for ventral (red,  $n=60$  cells in 8 embryos) and lateral (blue,  $n=99$  cells in 8 embryos) cells. (E-F) Error bars, s.e.m.

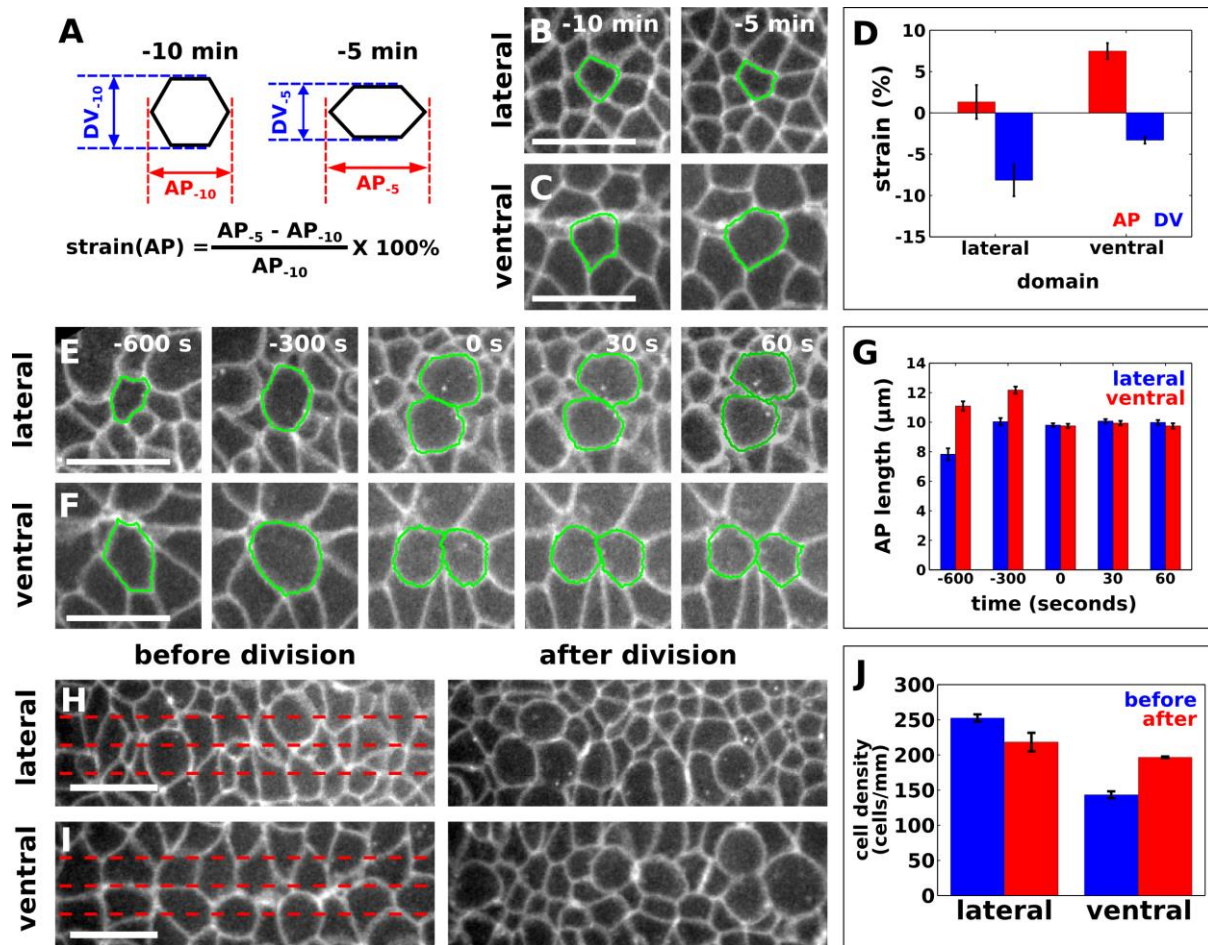


**Figure 5. Ventral divisions reduce AP strain by directionally increasing cell density.**

(A) Schematic showing strain calculation based on cell shape changes. (B-C) Lateral (B) and ventral (C) cells expressing Gap43:mCherry. Time is with respect the first ventral division. (D) AP and DV strain for both ventral (60 cells in 6 embryos) and lateral (49 cells in 5 embryos) cells. (E-F) Lateral (E) and ventral (F) cells expressing Gap43:mCherry. Time is with respect to their respective division. (G) AP length at different time points with respect to the time of division for lateral (blue,  $n = 19$  cells in 3 embryos before division, and 38 cells in 3 embryos after division) and ventral cells (red,  $n = 28$  cells in 3 embryos before division, and 56 cells in 3 embryos after division). (H-I) Images showing ventral (H) and lateral (I) cells expressing Gap43:mCherry, 5 minutes before completion of cell divisions in the field of view and 12 minutes later (H'-I'). AP cell density is the mean number of cells crossed by the three dashed red lines. (J) AP cell density for ventral ( $n = 5$  embryos) and lateral ( $n = 5$  embryos) regions. (B-C, E-F, H-I) Anterior, left. Bar, 20 μm. (D, G, J) Error bars, s.e.m.



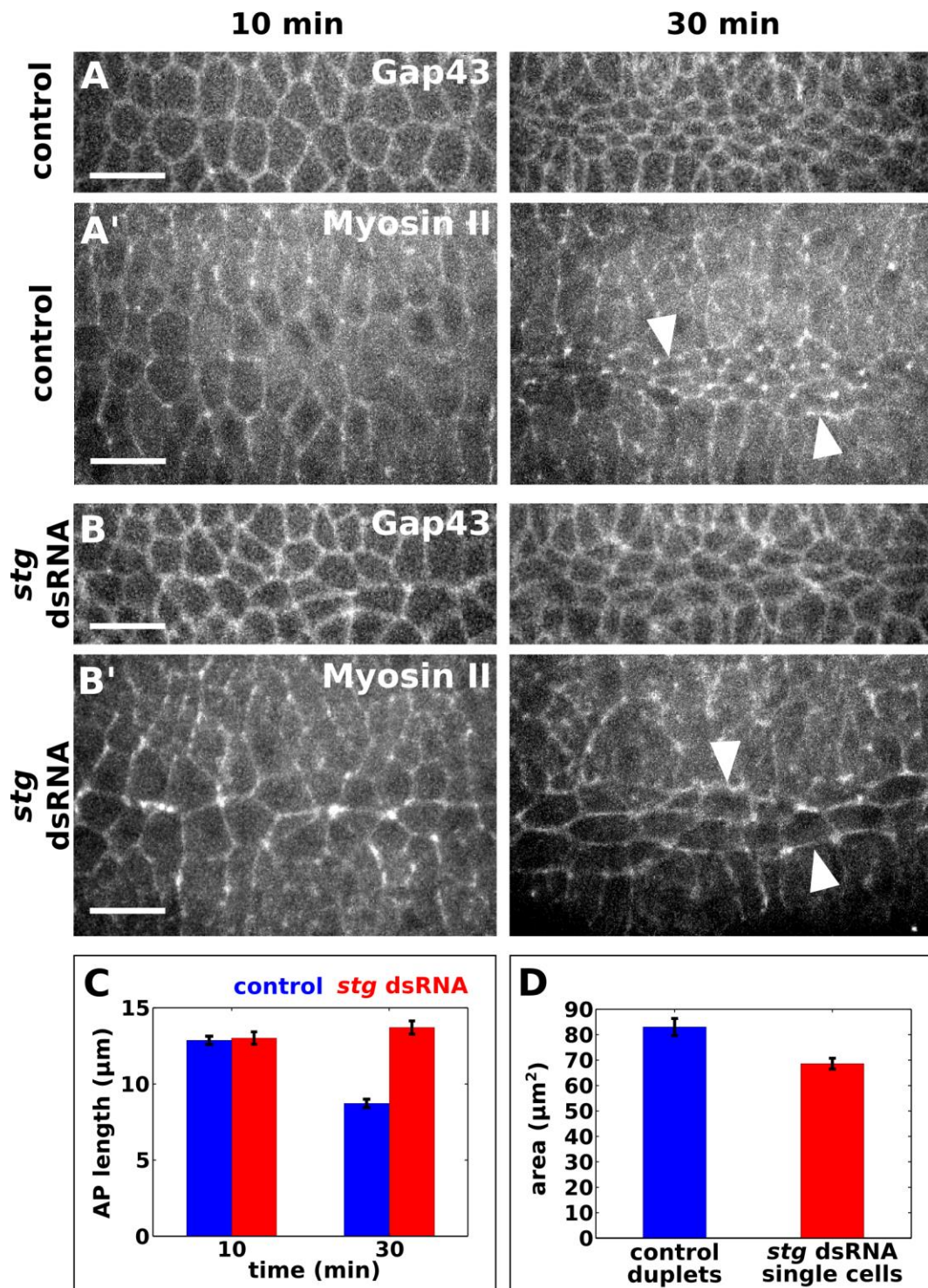


**Figure 6. Ventral divisions may increase mesectoderm surface area.** (A-B) Ventral cells expressing Gap43:mCherry (A-B) and Sqh:GFP (A'-B') in embryos injected with water (A) or *stg* dsRNA (B), 10 (left) and 30 min (right) after ventral furrow closure. Anterior, left. Bars, 20  $\mu\text{m}$ . Arrowheads indicate myosin accumulation in ventral cells. (C) AP cell length 10 and 30 minutes after ventral furrow closure in control (blue,  $n = 37$  cells in 4 embryos at 10 min, and 74 cells in 4 embryos at 30 min) and *stg* dsRNA (red,  $n = 40$  cells in 4 embryos)



embryos. **(D)** Area 30 min after ventral furrow closure for pairs of daughter cells in controls ( $n = 62$  pairs in 4 embryos) and single cells in *stg* dsRNA embryos ( $n = 68$  cells in 4 embryos) embryos. **(C-D)** Error bars, s.e.m.

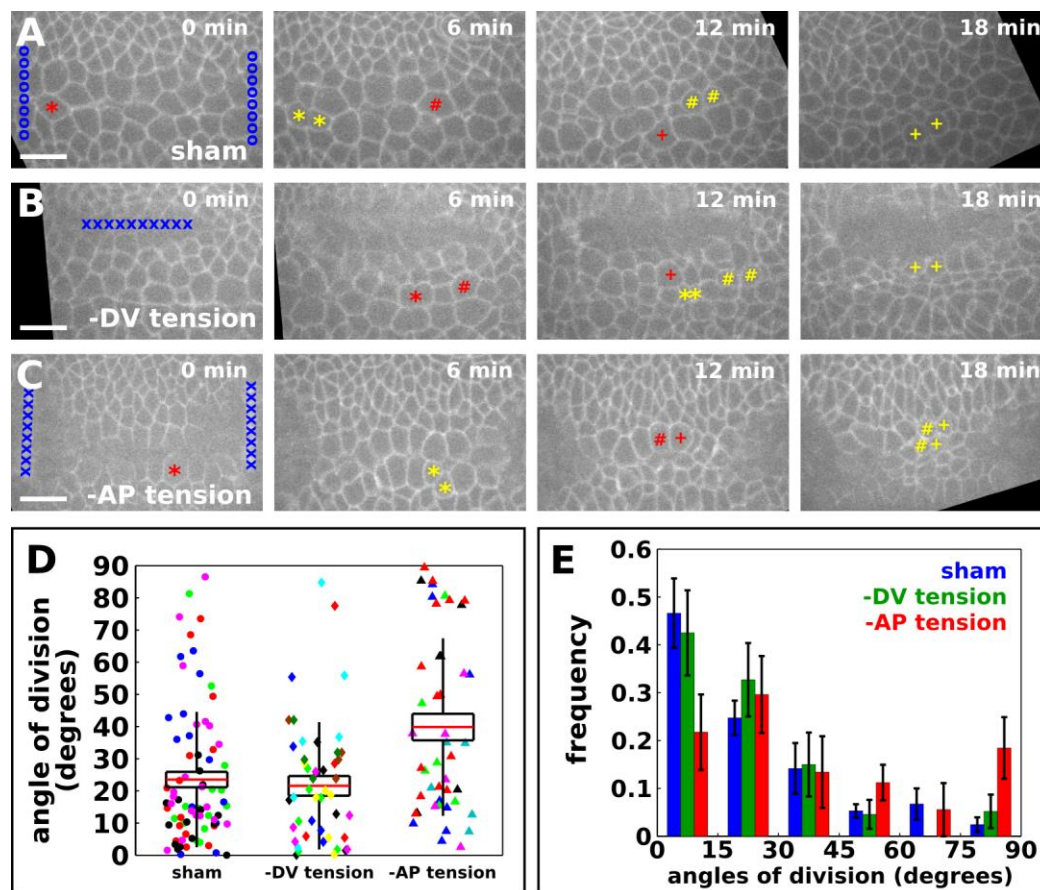


**Figure 7. Tension from the anterior and posterior poles is necessary for oriented cell divisions.** (A-C) Ventral cells expressing Gap43:mCherry after sham irradiation (A), ultraviolet irradiation to cause one incision parallel to the AP axis to mechanically separate ventral and intercalating cells (B, -DV tension), or two incisions parallel to the DV axis that isolate ventral cells from the anterior and posterior poles (C, -AP tension). Anterior left, ventral down. Bars, 20  $\mu$ m. Time is with respect to laser irradiation. Red symbols denote mother cells, yellow symbols indicate daughter cells. Blue shows the site of sham (circles) or ultraviolet (crosses) irradiation. (D-E) Cell division orientations relative to the ventral midline (D) and distributions (E) for sham-irradiated controls (blue in E), and embryos in which ventral cells were mechanically isolated from DV forces (green in E), or from AP forces (red in E).  $n = 77$  cells in 5 embryos for sham irradiation, 42 cells in 8 embryos for reduced DV tension, and 45 cells in 6 embryos for reduced AP tension. (D) Each symbol represents a cell division. Different colours indicate different embryos. Red lines, mean; box, s.e.m.; error bars, standard deviation (E) Error bars, s.e.m.

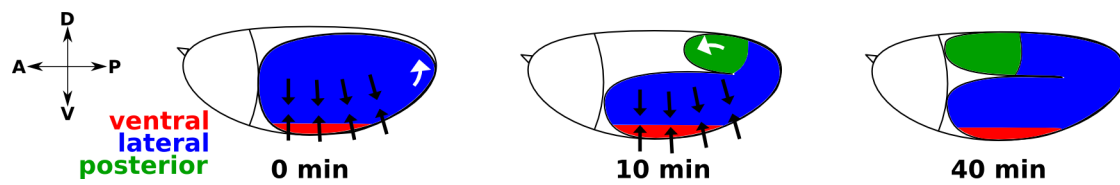


**Figure S1. Basic anatomy and mechanics of germband extension.** Cartoon depicting an embryo during early (left), mid (centre) or late (right) germband extension. The germband is coloured. Different colours indicate distinct cell populations: ventral (red), lateral (blue), and posterior (green). Anterior (A) left, posterior (P) right, dorsal (D) up, ventral (V) down. Black arrows indicate actomyosin-based contractile stresses generated in the germband. White arrows indicate tensile stresses caused by endoderm ingression in the posterior pole of the embryo.

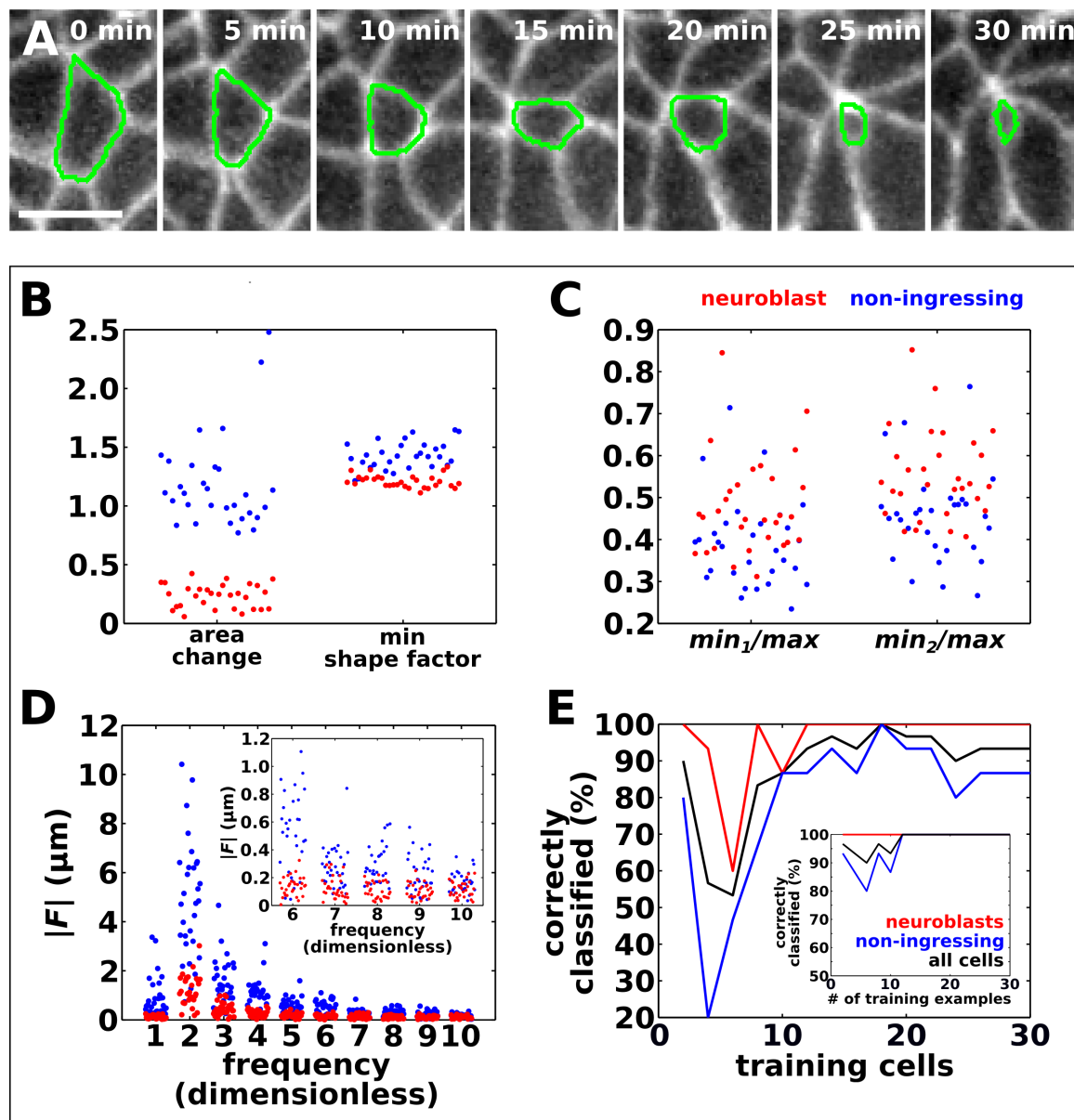
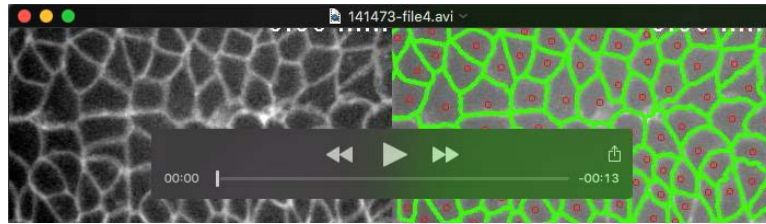
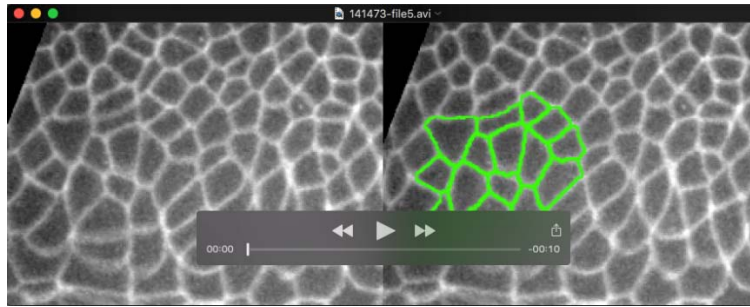


**Figure S2. Ingressing neuroblasts display distinct morphological features. (A)** Neuroblast expressing Gap43:mCherry as it delaminates from the ectoderm. Green shows segmentation results. Bar, 20  $\mu\text{m}$ . Anterior left, ventral down. **(B-D)** Scatter plots of the area change ratio and minimum shape factor (B), minimum-to-maximum cell radii ratios (C), and 1-10 integer components of the Fourier transform of the centroid-polygon distance (D) both for ingressing neuroblasts ( $n = 30$  in 10 embryos, red) and non-ingressing cells ( $n = 36$  in 10 embryos, blue). **(D)** Inset shows the magnitude of frequency components 6-10 with a different Y-axis scale. **(E)** Percent correctly classified neuroblasts (red), non-ingressing (blue), and total (black) cells as a function of the number of cells in the training set (in a 1:1 ratio of neuroblasts to non-ingressing cells). Inset shows percent correctly classified cells using only 6 features (area change, minimum shape factor,  $\min_1/\max$ ,  $\min_2/\max$ , and frequency components 1 and 2).

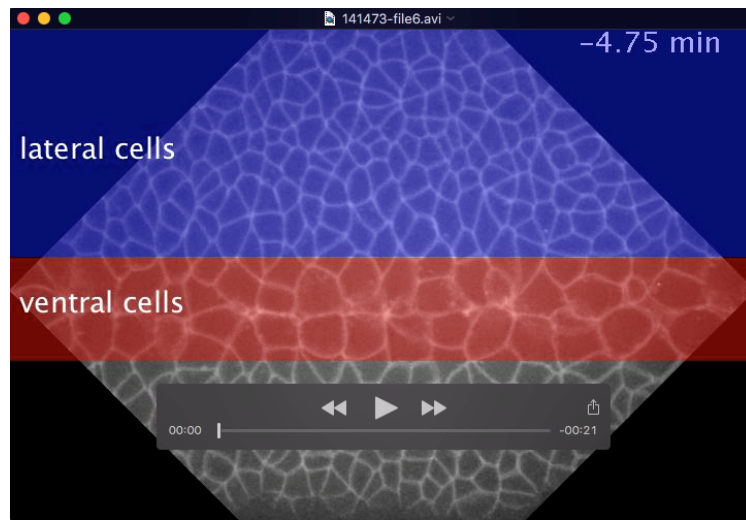


**Movie S1. Integrating image analysis and machine learning allows cell segmentation and tracking in developing embryos.** Germband cells expressing Gap43:mCherry at the final stages of axis elongation. Red circles represent watershed seeds. Green shows segmentation and tracking results. A stack was acquired every 15 s. Anterior left, ventral centre.

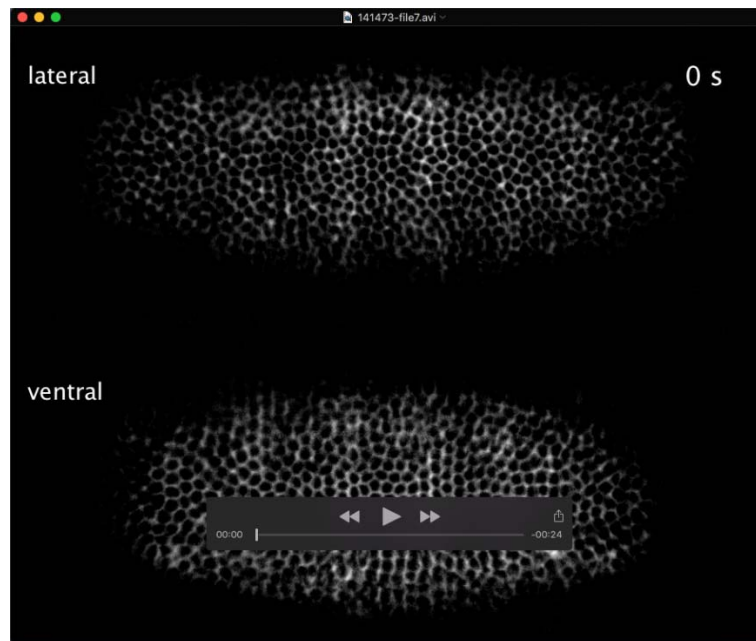


**Movie S2. Image analysis and machine learning can detect ingressing neuroblasts.**

Cells in a stage 7 embryo expressing Gap43:mCherry. Green represents segmentation and tracking results. Red indicates detection of a neuroblast. A stack was acquired every 15 s. Anterior left, ventral down.

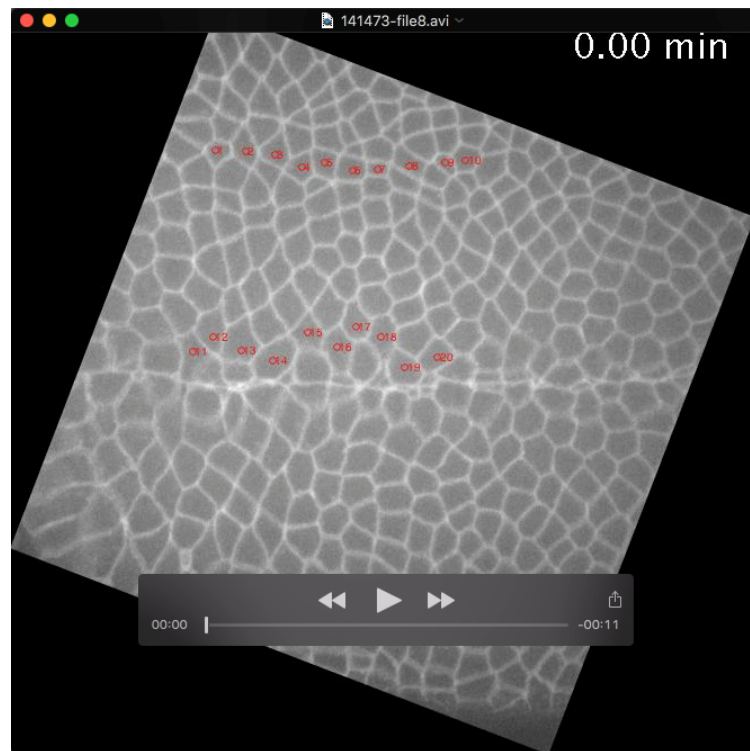


**Movie S3. Cells on the anterior end of the germband divide during *Drosophila* axis elongation.** Germband cells expressing Gap43:mCherry at the final stages of axis elongation. Red ventral, blue lateral. A stack was acquired every 15 s. Anterior left, ventral down.

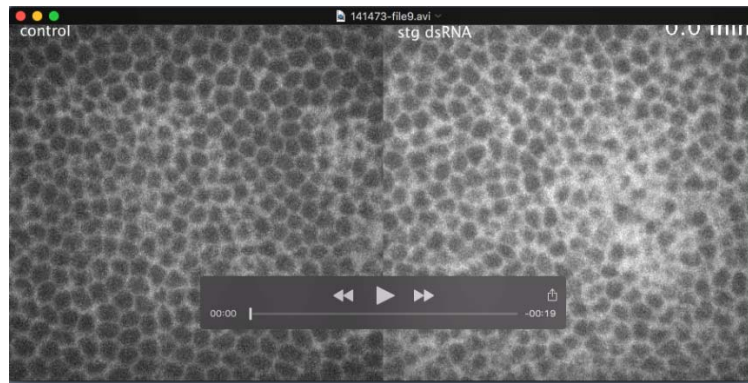


**Movie S4. Ventral cells divide at the same time as lateral cells.** Germband cells expressing Gap43:mCherry during axis elongation acquired using dual-illumination, light sheet microscopy. Cyan arrow indicates first lateral division, red arrow shows first ventral division. A stack was acquired every 25 s. Anterior left, ventral down (top) or centre (bottom).





**Movie S5. Ventral cells do not intercalate during axis elongation.** Germband cells expressing Gap43:mCherry during axis elongation. Red circles track cells. Cells 1-10 are lateral cells, cells 11-20 are ventral cells. A stack was acquired every 15 s. Anterior left, ventral down.



**Movie S6. *stg* dsRNA eliminates germband divisions.** Germband cells expressing Gap43:mCherry during axis elongation in a water-injected control (left) or an embryo injected with dsRNA against *stg* (right). A stack was acquired every 30 s. Anterior left, ventral down.

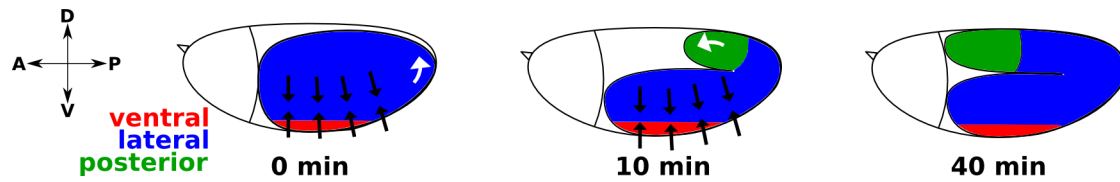


**Figure S1. Basic anatomy and mechanics of germband extension.** Cartoon depicting an embryo during early (left), mid (centre) or late (right) germband extension. The germband is coloured. Different colours indicate distinct cell populations: ventral (red), lateral (blue), and posterior (green). Anterior (A) left, posterior (P) right, dorsal (D) up, ventral (V) down. Black arrows indicate actomyosin-based contractile stresses generated in the germband. White arrows indicate tensile stresses caused by endoderm ingression in the posterior pole of the embryo.

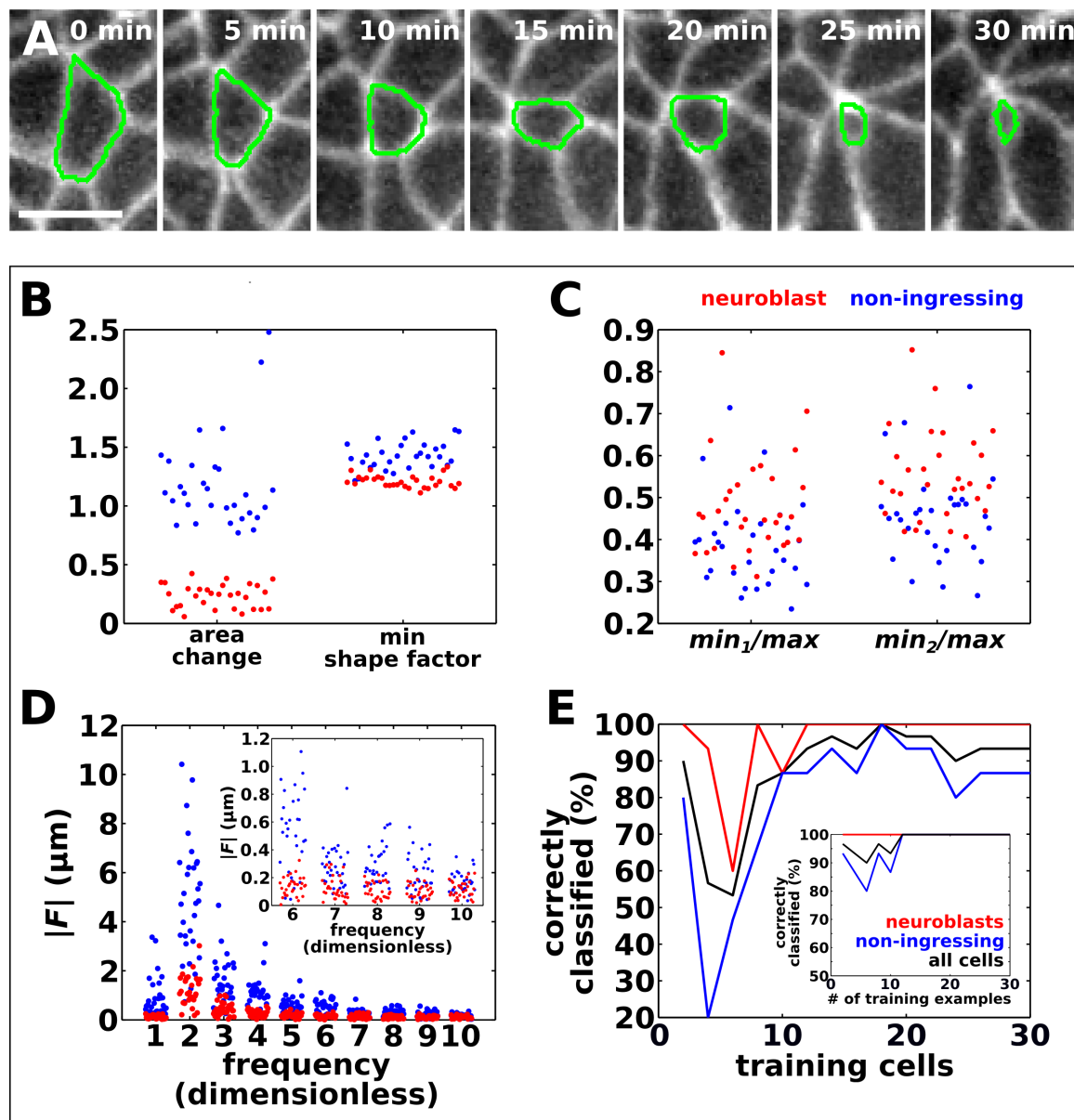
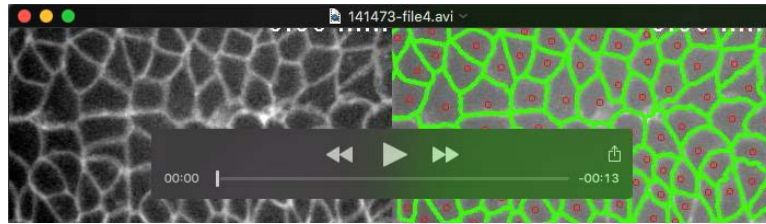
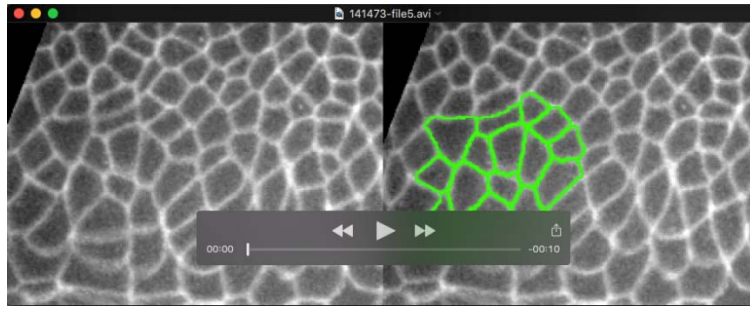


**Figure S2. Ingressing neuroblasts display distinct morphological features. (A)** Neuroblast expressing Gap43:mCherry as it delaminates from the ectoderm. Green shows segmentation results. Bar, 20  $\mu m$ . Anterior left, ventral down. **(B-D)** Scatter plots of the area change ratio and minimum shape factor (B), minimum-to-maximum cell radii ratios (C), and 1-10 integer components of the Fourier transform of the centroid-polygon distance (D) both for ingressing neuroblasts ( $n = 30$  in 10 embryos, red) and non-ingressing cells ( $n = 36$  in 10 embryos, blue). **(D)** Inset shows the magnitude of frequency components 6-10 with a different Y-axis scale. **(E)** Percent correctly classified neuroblasts (red), non-ingressing (blue), and total (black) cells as a function of the number of cells in the training set (in a 1:1 ratio of neuroblasts to non-ingressing cells). Inset shows percent correctly classified cells using only 6 features (area change, minimum shape factor,  $min_1/max$ ,  $min_2/max$ , and frequency components 1 and 2).

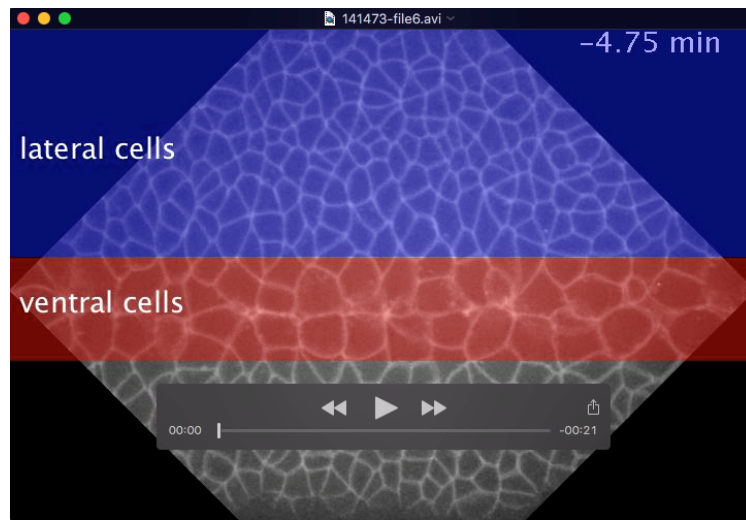


**Movie S1. Integrating image analysis and machine learning allows cell segmentation and tracking in developing embryos.** Germband cells expressing Gap43:mCherry at the final stages of axis elongation. Red circles represent watershed seeds. Green shows segmentation and tracking results. A stack was acquired every 15 s. Anterior left, ventral centre.

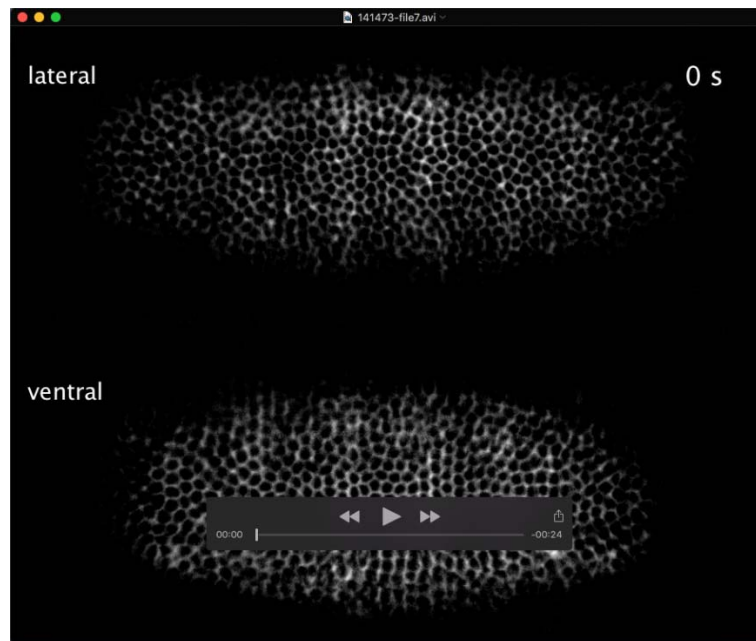


**Movie S2. Image analysis and machine learning can detect ingressing neuroblasts.**

Cells in a stage 7 embryo expressing Gap43:mCherry. Green represents segmentation and tracking results. Red indicates detection of a neuroblast. A stack was acquired every 15 s. Anterior left, ventral down.

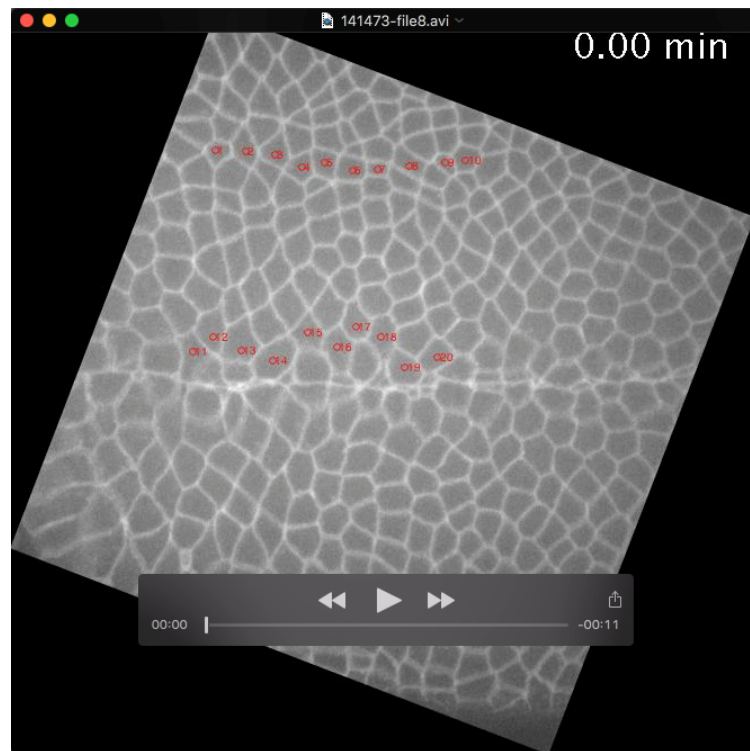


**Movie S3. Cells on the anterior end of the germband divide during *Drosophila* axis elongation.** Germband cells expressing Gap43:mCherry at the final stages of axis elongation. Red ventral, blue lateral. A stack was acquired every 15 s. Anterior left, ventral down.

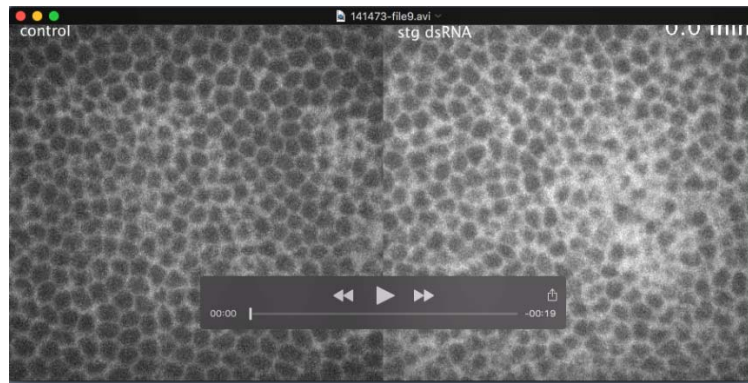


**Movie S4. Ventral cells divide at the same time as lateral cells.** Germband cells expressing Gap43:mCherry during axis elongation acquired using dual-illumination, light sheet microscopy. Cyan arrow indicates first lateral division, red arrow shows first ventral division. A stack was acquired every 25 s. Anterior left, ventral down (top) or centre (bottom).





**Movie S5. Ventral cells do not intercalate during axis elongation.** Germband cells expressing Gap43:mCherry during axis elongation. Red circles track cells. Cells 1-10 are lateral cells, cells 11-20 are ventral cells. A stack was acquired every 15 s. Anterior left, ventral down.



**Movie S6. *stg* dsRNA eliminates germband divisions.** Germband cells expressing Gap43:mCherry during axis elongation in a water-injected control (left) or an embryo injected with dsRNA against *stg* (right). A stack was acquired every 30 s. Anterior left, ventral down.